Correspondence to:
A. Kirincich,
akirincich@whoi.edu

Horizontal Stirring Over the Northeast U.S. Continental Shelf: The Spatial and Temporal Evolution of Surface Eddy Kinetic Energy

Anthony Kirincich[1] [ID]**, Ben Hodges[1], Pierre Flament[2], and Victoria Futch[3]** [ID]

[1]Woods Hole Oceanographic Institution, Woods Hole, MA, USA, [2]University of Hawaii at Manoa, Honolulu, HI, USA, [3]United States Coast Guard Academy, New London, CT, USA

Abstract This study examines the spatial and temporal variability of eddy kinetic energy over the Northeast Shelf using observations of surface currents from a unique array of six high frequency radar systems. Collected during summer and winter conditions over three consecutive years, the horizontal scales present were examined in the context of local wind and hydrographic variability, which were sampled concurrently from moorings and autonomous surface vehicles. While area-averaged mean kinetic energy at the surface was tightly coupled to wind forcing, eddy kinetic energy was not, and was lower in magnitude in winter than summer in all areas. Kinetic energy wavenumber spectral slopes were generally near $k^{-5/3}$, but varied seasonally, spatially, and between years. In contrast, wavenumber spectra of surface temperature and salinity along repeat transect lines had sharp k^{-3} spectral slopes with little seasonal or inter-annual variability. Radar-based estimates of spectral kinetic energy fluxes revealed a mean transition scale of energy near 18 km during stratified months, but suggested much longer scales during winter. Overall, eddy kinetic energy was unrelated to local winds, but the up- or down-scale flux of kinetic energy was tied to wind events and, more weakly, to local density gradients.

Plain Language Summary This study uses ocean currents observed over a 10,000 km² area south of Massachusetts and Rhode Island to examine the size of the eddies that stir the coastal ocean. An array of land-based high frequency radar systems remotely measured surface currents at high resolution, while moored and mobile instruments measured surface winds, ocean temperatures, and salinities. The observed eddies were more energetic during summer, when surface waters were less dense than bottom waters, than during winter, when the ocean was well mixed. In the eastern portion of the study area, near a shallow submarine bank, the amount of energy contained in eddies increased with the size of the eddy at a rate predicted by theories of ocean mixing. In the western region, the energy of larger eddies was smaller, likely due to the local coastline limiting the size of these features. Energy levels observed in surface temperature and salinity measurements were similar to satellite-based estimates, but had little seasonal variability, suggested rapid horizontal mixing was occurring over the shelf. The transfer of energy between eddies of different sizes varied on short 3–10 days timescales, in part as a response to wind events, as well as the transport of density gradients.

1. Introduction

Recent advances in remote sensing of oceanic surface currents have revealed dramatic examples of both persistent and transient small-scale O(<20 km) features in proximity to the coast (i.e., Figure 1 Chavanne et al., 2010; Kim, 2010; Kirincich et al., 2013; Kirincich, 2016a). With horizontal lengthscales similar to the internal deformation radius, and O(1) Rossby numbers, these coherent vortices and frontal features represent a class of lateral exchange processes that are not well characterized within the coastal ocean. Though mesoscale and sub-mesoscale dynamics have been studied in the open ocean for some time (see McWilliams, 2016, for a review), the combined influence of bottom stress, topography, winds, and stratification on features near the coast render them dynamically distinct from open ocean submesoscale flows (Mahadevan & Tandon, 2006; Mcwilliams, 1985; McWilliams, 2009) and from purely bathymetrically forced features (McCabe et al., 2006; Signell & Geyer, 1991).

Both the dynamics of coastal submesoscale features and their role in driving the exchange of water and materials across the shelf are poorly understood. Over wide continental shelves, such as the Mid-Atlantic Bight stretching from Cape Hatteras to Cape Cod along the U.S. east coast, ocean heat budgets have uncertainties that suggest unresolved across-shelf eddy heat fluxes (Lentz, 2010). Efforts focused on the inner part of the shelf (i.e., water depths less than 30 m, Ganju et al., 2011; Kirincich et al., 2013; Fewings & Lentz, 2011; Kirincich & Lentz, 2017)
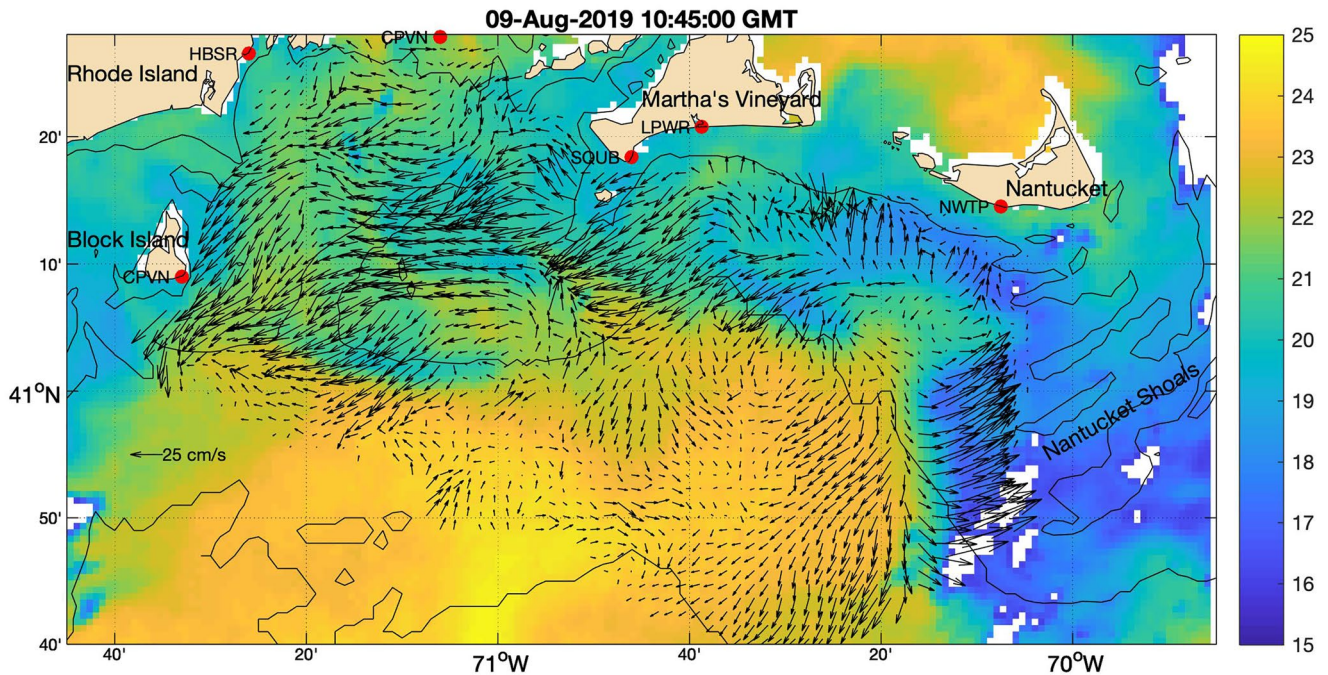
Figure 1. The Northeast Shelf (NES) of the United States offshore of Southern New England from Block Island, in the west, to Nantucket, in the east, with the (black lines) 20, 40, and 60-m isobaths and (red dots) installed HFR systems shown. Vectors represent the residual surface currents–a tidal fit has been removed from each 2-km grid point using T_Tide (Pawlowicz et al., 2002) – on 9 August 2020 at 10:45 GMT. Color indicates concurrent sea surface temperature (SST) from AVHRR.

have suggested that coastal mesoscale and submesoscale dynamics can have a significant impact on exchange budgets between the nearshore (Sinnett & Feddersen, 2014) and areas offshore. Yet, these features have been difficult to resolve, particularly over broad, shallow shelves, as the horizontal scales of interest (2–20 km) are smaller than the resolutions of most existing observing systems. As a result, the temporal and spatial scales of mixing and exchange, often represented by an eddy diffusivity (i.e., Sundermeyer & Ledwell, 2001), are not well constrained in coastal environments (Rypina et al., 2016).

This study examines the coastal mesoscale and sub-mesoscale variations present over the middle part of the Northeast Shelf (Figure 1) offshore of Southern New England, using observations from a unique system of land-based high frequency radars (HFRs) combined with in situ sampling of hydrography and winds from moored and mobile sensors. The critical scales of horizontal stirring are evaluated through the lens of the eddy kinetic energy (EKE), its wavenumber spectrum, and estimates of spectral kinetic energy (KE) fluxes. Heavily utilized in studies of open ocean submesoscale currents (Arbic et al., 2013; Brannigan et al., 2015; Callies et al., 2015; Spiro Jaeger et al., 2020; Thompson et al., 2016), wavenumber statistics of the surface variability (e.g., Denman & Abbott, 1994; Capet et al., 2008a; Callies & Ferrari, 2013) can be useful for identifying the lengthscales that dominate exchange as well as the underlying dynamics present. As shown in previous efforts (Soh & Kim, 2018; Yoo and Kim, 2018), aggregating the vast amounts of observational data provided by HFRs using KE analyses can simplify identification of the critical scales, the direction of energy transfer (Arbic et al., 2013), and the type of diffusive regime (Rypina et al., 2014) present within the flow field.

As shown below, the observations allow the seasonal and spatial variations of mean and eddy kinetic energy at the surface to be captured using an analysis of transects through the study area. Variations in the energy cascade are diagnosed from changes in the spectral flux of KE over time, enabling a discussion of the potential dynamical drivers of the flow field and their implications. Additional details on horizontal stirring in the region and the EKE wavenumber spectrum as a tool for understanding ocean dynamics are presented first, followed by details of the observations and analysis methods.

2. Background

2.1. Horizontal Stirring and Eddy Kinetic Energy

Open ocean mesoscale variability is typically defined to occur at scales greater than the internal deformation radius, with submesoscale variability thus defined as smaller scales having significant ageostrophic components and high Rossby numbers (Mahadevan & Tandon, 2006). In the coastal ocean, with mixed layer depths of 5–15 m and density differences of 2–3 kg m^{-3} during stratified periods, the baroclinic deformation radii –the scale thought to separate mesoscale and submesoscale processes – should then be 2–5 km. However, recent observations (Kim, 2010; Kirincich, 2016b; Kirincich & Lentz, 2017) have found coherent features with O(1) Rossby numbers at broader range of scales (1–20 km), suggesting that a separation of scales may not exist over the shelf.

The structures that define submesoscale variability - including squirts, jets, eddies, and fronts (e.g., Figure 1) - are far more commonly seen in the ocean via remote sensing of temperature (e.g., DiGiacomo & Holt, 2001; Ullman & Cornillon, 2001) than via velocity observations. Field observations of submesoscale currents have been limited to isolated studies of intense fronts on the edge of oceanic features (Flament & Armi, 2000; Paduan & Niiler, 1990), analysis of hydrographic or drifter observations (D'Asaro et al., 2018; Mcwilliams, 1985), or aggregates of sparse shipboard transects (Callies & Ferrari, 2013; Rocha et al., 2016). More common are theoretical developments (Callies & Ferrari, 2013), which have attempted to link statistics of the flow field, namely the shape of the kinetic energy wavenumber spectrum (WNS) or the spectral flux of kinetic energy, to the dynamical processes present in the ocean. For example, in mesoscale geostrophic or quasi-geostrophic horizontal turbulence, surface velocities have spectral slopes of k^{-3}, while theories of submesoscale surface horizontal turbulence predict slopes of $k^{-5/3}$ (Mahadevan & Tandon, 2006). In this manner, the kinetic energy WNS may serve as a diagnostic test for the types of instability processes acting to stir the ocean laterally. However, small-scale, eddy-driven energy fluxes can be significant in the coastal ocean (Capet et al., 2008a), giving rise to spectral slopes quite different from those associated with mesoscale energy cascades.

Close to the coast and in areas of strong tides, bathymetry plays a defining role in the creation of small-scale features, with intense headland eddies (McCabe et al., 2006; Signell & Geyer, 1991) or instabilities of tidal mixing fronts (Brink, 2012) generating circulation variability. Further offshore, where the effects of bottom friction might be reduced due to increased stratification, observations suggest that sub-tidal, density-driven processes dominate eddy creation (Kim, 2010; Yoo and Kim, 2018). Baroclinic instabilities were effective eddy-generating mechanisms in model studies of upwelling and downwelling fronts (Brink, 2015; Brink & Seo, 2015) and continental slope flows (Bracco et al., 2016). However, strain-driven frontogenesis (Capet et al., 2008a; Hoskins & Bretherton, 1972; Hoskins & West, 1979), nonlinear Ekman effects (Flament & Armi, 2000; Mahadevan et al., 2008; Thomas et al., 2008), or a series of smaller instability mechanisms (Barth, 1994; Durski & Allen, 2005; Mahadevan & Tandon, 2006; Molemaker et al., 2005) also lead to submesoscale features. Regardless, features on scales of kilometers tend to have high rates of lateral strain, large relative vorticities, significant ageostrophic components (Mahadevan & Tandon, 2006), and the potential to dominate the lateral exchange of water masses and particles across the shelf.

In the past two decades, land-based remote sensing via HFRs has been used to examine the velocity fields of coherent vortices, or eddies, in coastal environments (Beckenbach & Washburn, 2004; Chavanne et al., 2010; Kim, 2010; Kirincich, 2016b; Kirincich & Lentz, 2017; Nencioli et al., 2010), finding both persistent and highly transient features at scales as small as the resolution of the observations. Kim et al. (2011) and Soh and Kim (2018) were the first to examine the statistics of submesoscale flows, including spectral slopes and energy decay, using HFR observation. Limited to short range (40 km) HFR systems in deep water coastal environments, both found that mean spectral slopes in wavenumber space tended to roll-off at k^{-3} before flattening at the shortest lengthscales observed (2–4 km as a function of the data processing methods). At longer lengthscales (smaller wavenumbers), slopes were less than or equal to $k^{-5/3}$. Both works interpreted these results to suggest that breaks between areas of constant slope were dynamical regime shifts that controlled the upscale or downscale flux of kinetic energy.

In contrast, high resolution model results in similar coastal conditions (Capet et al., 2008a) suggest that the spectral slopes of velocity should be flat at the scales at which energy is input, before rolling off at $\sim k^{-2}$ up to the effective resolution of the model, where the slopes steepen. The flux of kinetic energy within the kinetic energy budget, defined in the literature as $\Pi(k)$ where k is the total wavenumber (Scott & Wang, 2005), provides an
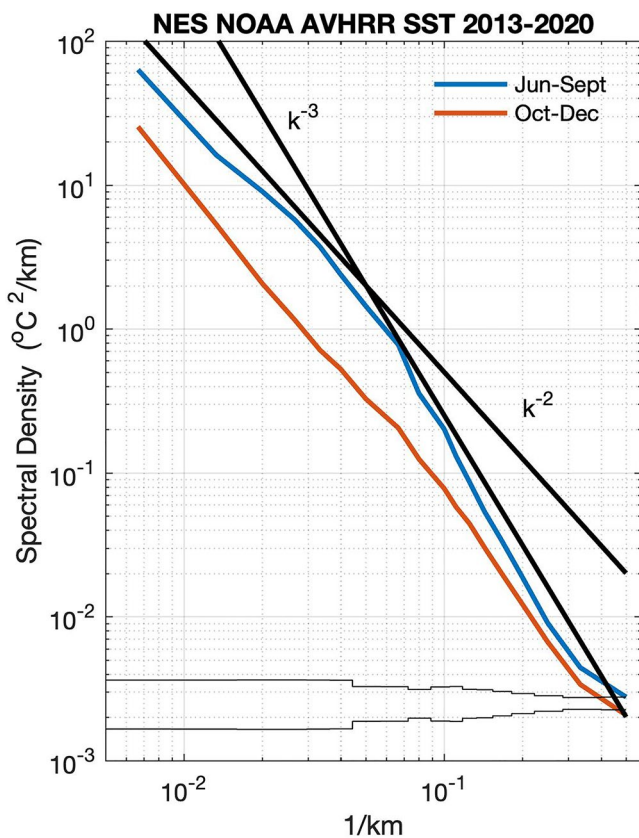
Figure 2. Area-averaged, seasonally averaged (July-September and October-December) along-isobath wavenumber spectra for 1-km resolution AVHRR SSTs (obtained via the University of Delaware, http://basin.ceoe.udel.edu/thredds/catalog.html) in water depths of 38–55 m over the NES during 2013–2020, with 100–150 cloud-free images available for each year. Spectral slopes of k^{-2} and k^{-3} are shown in black for reference, while confidence intervals for the spectral bin averages are shown below.

additional assessment of the scales at which energy is input into the coastal ocean. Estimated spectrally, $\Pi(k)$ can also reveal the lengthscale at which energy in the flow field transitions from moving downscale (to smaller scales) to upscale (to larger scales) (Arbic et al., 2013; Clary et al., 2019; Scott & Wang, 2005).

2.2. Submesoscale Variability Over the Northeast Shelf

The Northeast Shelf (NES: Figure 1) has been the site of a number of observational programs, including studies focused at the shelfbreak, for example, the Shelf Edge Exchange Processes (SEEP: Aikman & Ou, 1988) and Shelfbreak Primer (Fratantoni & Pickart, 2003), as well as studies focused inshore, for example, Nantucket Shoals Flux Experiment (NSFE: Beardsley et al., 1985), Coastal Mixing and Optics (CMO: Dickey & Williams, 2001), or Coupled Boundary Layers Air-Sea Transfer (CBLAST: Edson et al., 2007). The region is representative of "wide-shelf" coastal ocean environments, having a broad and flat shelf, a well-defined and distinct shelf break, forcing by both wind and buoyancy, and spatially varying coastlines and tidal currents. To the east, waters over the shallow Nantucket Shoals are vertically well mixed, and cooler throughout the year (Figure 1; Limeburner & Beardsley, 1982; He & Wilkin, 2006), while the waters to the west undergo a seasonal cycle of stratification (Figure 4, Lentz et al., 2008). During winter, mid-shelf waters are vertically well mixed to depths greater than 60 m, but can have significant horizontal density gradients as a result of differential cooling and mixing, as well as across-shelf salinity gradients.

Submesoscale currents over the NES, and other wide continental shelves, should differ substantially from narrow shelf environments (Capet et al., 2008a; Romero et al., 2013; Yoo and Kim, 2018), as the influence of the bottom and seasonal changes in stratification are larger over wide shelves. Cloud-free, 1-km resolution AVHRR SST observations of the NES suggest that the largest horizontal gradients present in any season are the cool water features advected west from Nantucket Shoals, approximately along-isobath (Figure 1). At the surface, temperature variability at submesoscales appears to reach a peak in summer (Figure 2), where an 8-year average of available along-isobath SST data reveals a change in spectral slope during summer at around 20 km from k^{-2} to k^{-3}. Although a range of scales can be seen in SST imagery during weakly stratified winter periods (not shown here), SST observations during winter have no similar change in spectral slope (Figure 2). In the region, the scalar variance generated by the large horizontal gradients in the eastern part of the NES are substantially reduced by the time shelf waters reach the western edge (e.g., Figure 1), suggesting that significant horizontal mixing occurs in the region between.

2.3. Potential Impacts

Horizontal stirring at submesoscales is directly linked to both the magnitude and the lengthscale dependence of lateral eddy diffusivity over the shelf (i.e., Capet et al., 2008b; Brink, 2015). By analogy with molecular diffusion, the efficiency of eddies in transporting tracers has been conventionally represented by lateral turbulent or eddy diffusion, to account for the un- and under-resolved scales of motion in both observations and numerical models (see LaCasce, 2008, for a review). Observational tests of eddy diffusivity in the coastal ocean have found widely varying results. Estimates from drifter or dye release studies (e.g., Sundermeyer & Ledwell, 2001; Spydell et al., 2007; Rypina et al., 2014) as well as a hybrid analysis of HFR, drifter, and dye results (Rypina et al., 2016) have shown order of magnitude variability over short time scales, non-isotropic spreading, and generally larger magnitudes than the Okubo (1971) scaling for similar spatial scales. Ferrari and Nikurashin (2010) suggest that such variability in eddy diffusivity is shaped by variations in the eddy kinetic energy at those scales.

Table 1
HFR Stations and Coverage by Year

Location	Nantucket, MA	Tisbury,MA	Chilmark,MA	Westport,MA	Narragansett,RI	Block Island, RI
ID	NWTP	LPWR	SQUB	HBSR	CPVN	BKIL
Latitude (°N)	41.2417	41.3458	41.3065	41.5083	41.4417	41.1500
Longitude (°W)	70.1250	70.6458	70.7675	71.1000	71.4333	71.5500
Operator	WHOI	WHOI	WHOI	WHOI	WHOI	URI
HFR Type	UH-HFDR	UH-HFDR	SeaSonde	UH-HFDR	UH-HFDR	SeaSonde
Frequency (MHz)	16	16	25	16	16	25
Range Resolution (km)	2	2	1	2	2	1
Temporal Coverage						
2018	July-Dec	July-Dec	July-Dec			
2019	July-Dec	July-Dec	July-Dec	Aug-Dec	Aug-Dec	Aug-Dec
2020	Oct-Dec	Oct-Dec	Oct-Dec	Oct-Dec	Oct-Dec	Oct-Dec

While previous results focused on the inner part of the shelf have examined the local transport of water masses dominated by depth-dependent across-shelf exchange flows driven by wind forcing (see Lentz & Fewings, 2012, for a review), the eddy-driven lateral exchange that likely occurs at submesoscales is both a critical component of exchange and poorly resolved. In a study by Kirincich and Lentz (2017), the effects of O(1–5 km) eddies in the inner shelf resulted in exchange equivalent to half the wind-driven, depth-dependent exchange and significant across-shelf heat flux. Over the shelf as a whole, both model (Wilkin, 2006) and observational (Lentz, 2010) results suggest that lateral, or "eddy" advection has a cooling effect on the shelf, removing as much as half of the seasonal temperature increase that would be produced by the surface fluxes alone. Thus, improved in situ esti-mates of the eddy fluxes driven by the energy cascade (i.e., Capet et al., 2008b) are necessary to further constrain budgets of basic water properties over the shelf, particularly as the data availability from SST imagery is not sufficient to understand the time dependence of the fluxes.

3. Data and Methods

3.1. Observations

This study examines the space and time scales of eddy kinetic energy over the wide, shallow, NES using a novel implementation of HFR to achieve spatial and temporal resolutions sufficient to capture the horizontal scales of velocity variability. SST imagery (Figures 1 and 2) suggests that most features of interest over the mid-shelf have scales of 4–40 km but can evolve over tidal timescales; thus, HFR observations with both radial and azimuthal resolutions of 2 km up to 80–90 km offshore at hourly timescales are necessary to resolve the evolution of submesoscale features and their dynamics. Toward this measurement goal, a series of four multi-antenna HFRs built by the University of Hawaii (described by Kirincich et al., 2019) were deployed in the region and augmented by two existing high resolution SeaSonde HFRs deployed previously with funding from NOAA-IOOS (Figure 1; Table 1). Using a grid of 8 separate receive antennas, the UH systems maximize both the temporal and azimuthal resolution of surface currents over a wide area (see Kirincich et al., 2019, for details), producing fully independ-ent, 30-min averages of high-resolution (2-km everywhere), low error, surface currents over a 150×80 km area. RMS differences of the system against in situ observations were 5–7 cm s^{-1} (see Appendix A for details).

The HFR observations, deployed between spring 2018 and summer 2019, were paired with detailed, in situ observations of hydrography, currents, and winds during three separate study periods, spanning June to Decem-ber of 2018 and 2019, and October to December of 2020. For the two 6-month periods in 2018 and 2019, a trio of surface moorings and one subsurface mooring were deployed in the center of the eastern HFR coverage area (Figure 3, Table 2) The central surface mooring, stationed along the 40-m isobath, hosted a Vaisala WXT520 weather station and 8 temperature-conductivity (CT) sensors (SBE37 Microcats) spread throughout the water column. A nearby subsurface mooring supported upward- and downward-looking ADCPs to collect high reso-lution velocity profiles of the top 8 m of the water column and coarser resolution velocity profiles of the lower
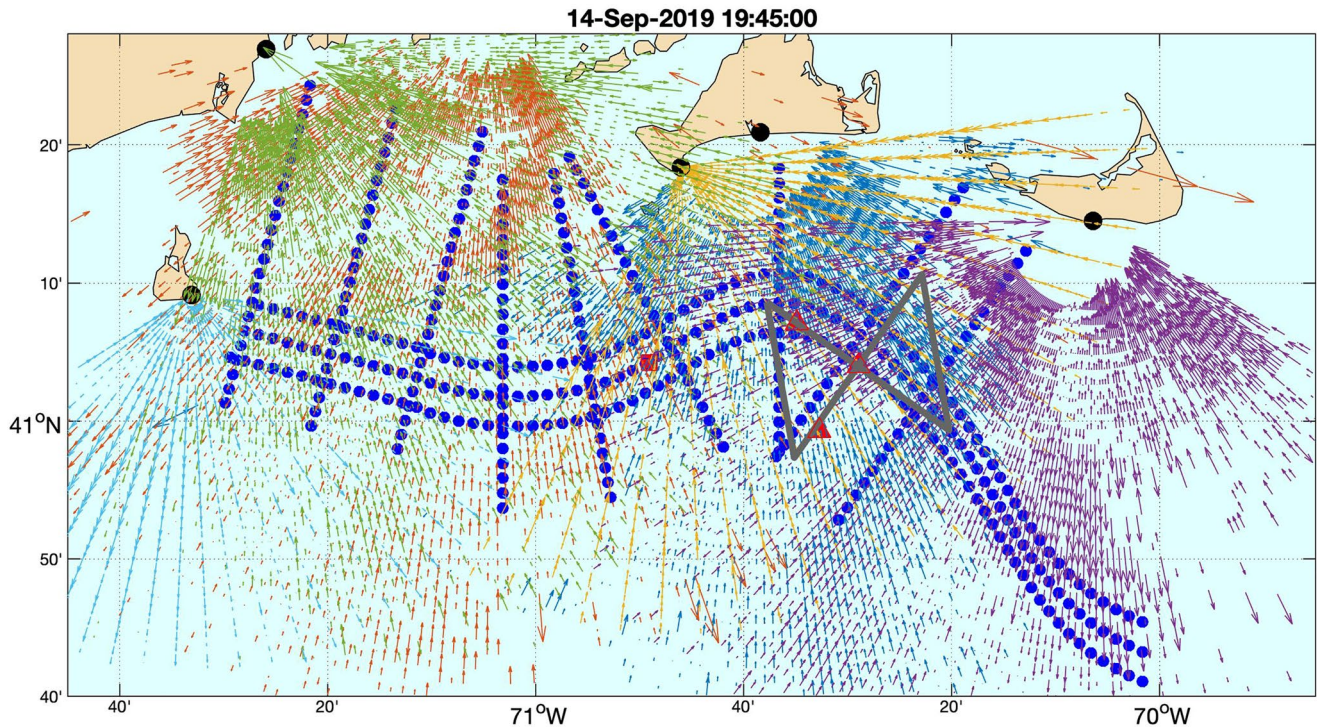
Figure 3. A snapshot of the radial velocities from all sites on 14 September 2019, and the along- and across-shelf analysis lines used for estimating wavenumber spectra (blue dots). Mooring locations from the 2018 and 2019 deployments (red triangles), the Wave Glider track-lines (gray), and 2020 mooring location (red square at 70° 50' W) are also shown. The eastern, central, and western across-shelf analysis lines used in Figures 7 and 8 are shown here as the eastern, central, and western three across-shelf lines (blue dots) respectively.

30 m of the water column. The two additional flanking surface moorings, each with 7 CT sensors, were located 10 km away in both the across- and along-shelf (2018 only) directions, allowing estimates of the depth-dependent lateral hydrographic gradients. During an additional 3-month period in fall 2020, a single mooring pair, similar to the central surface and sub-surface moorings described above, was deployed further west near the 40-m isobath (Figure 3, Table 2). Data from all moored sensors were processed from their raw sampling rates (Table 2), quality controlled using standard methods (*Kirincich and Lentz*, 2017), and averaged onto the 30-min time interval of the HFR currents.

Finally, two WHOI-owned, Liquid Robotics SV2 Wave Glider autonomous surface vehicles were deployed for 3-month periods during both 2018 and 2019 to collect along-track observations of winds and surface hydrography. Outfitted with SeaBird CTDs at water depths of 0.3 and 6.5 m, the Wave Gliders followed a butterfly shaped regular survey pattern (Figure 3), allowing repeated sampling of horizontal gradients of temperature and salinity within the surface layer at multiple scales around the mooring locations. With transit speeds of 0.5–1 m/s, Wave Gliders are 3–5 times faster than Slocum-type gliders, allowing O(10 km) features to be sampled on timescales of 2–4 hr. Combined, the Wave Glider surveys sampled each transect line approximately once per day and were used to estimate scalar variances following Appendix B.

3.2. Wavenumber Spectra

EKE wavenumber spectra (WNS) were estimated on the along- and across-isobath lines shown in Figure 3. Along- and across-isobath lines were chosen – over a uniform 2-km gridded product (Figure 1) – to both represent the prevailing along-isobath currents over the longest distance possible (~150 km), as well as sample the potentially changing across-shelf conditions from east to west. Three independent along-shelf lines, centered at the 40-m isobath throughout most of the domain were used as AVHRR SST imagery suggested the 40-m isobath was the location of the highest spatial gradients in surface temperature, along with three across-shelf lines in each
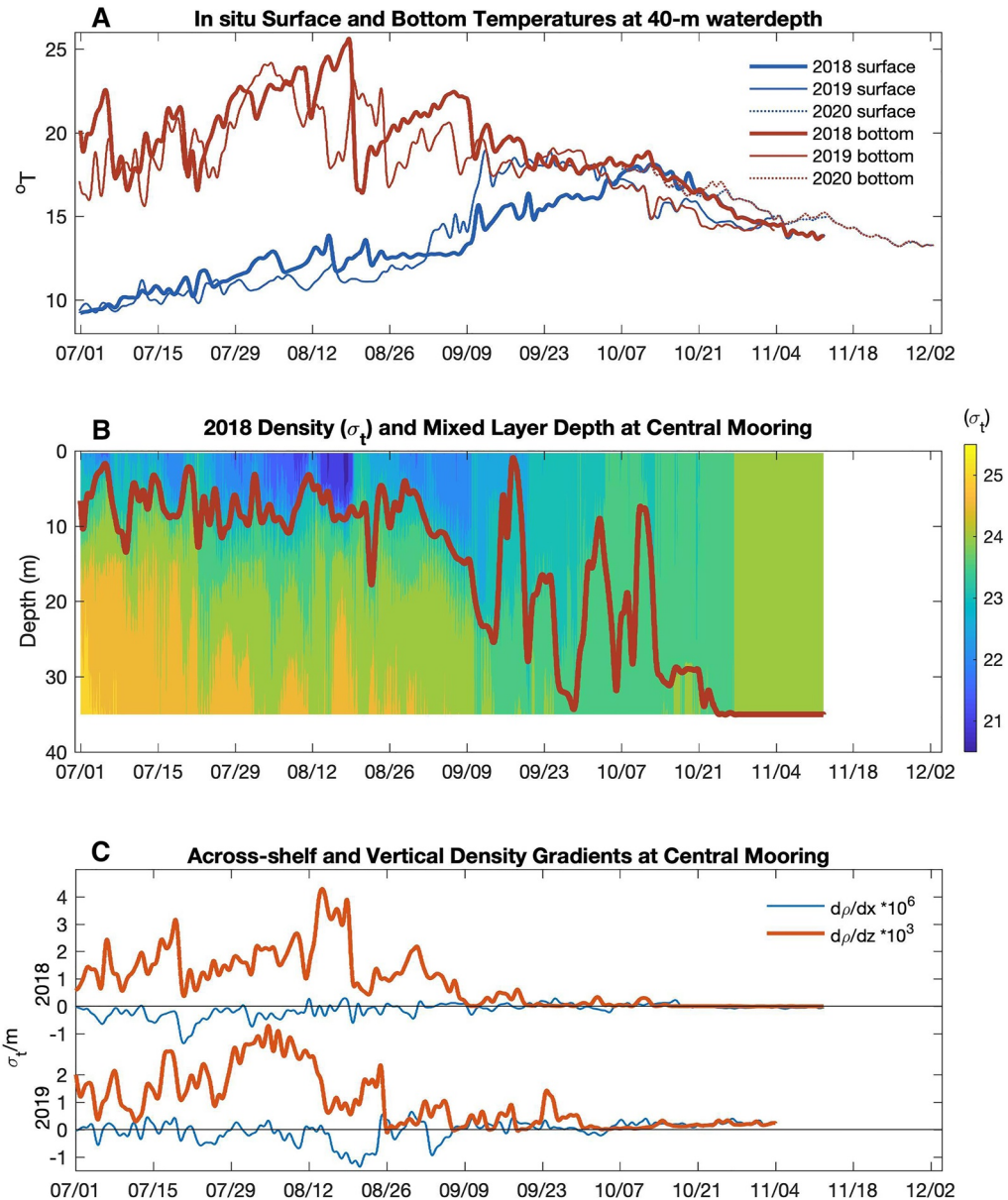
Figure 4. (a) In situ top (red: 0.6 m depth) and bottom (blue: 35-m depth) water column temperatures during 2018–2020. (b) Low-pass filtered potential density for 2018, interpolated from the 8 CTs deployed from 0.6 to 35 m depth and (red) low-pass filtered mixed layer depth, estimated from the potential density profiles as the depth at which the density is 0.1 kg/m^3 greater than the surface density. (c) Observed vertical ($d\rho/dz$) and horizontal ($d\rho/dx$) density gradients at the central mooring for 2018 and 2019.

of the eastern, central, and western areas (Figure 3). Other line orientations yielded qualitatively similar results to those presented here.

For evenly spaced 2-km locations–the maximum resolution of the radial velocities–along each line, raw data from non-overlapping 30 min periods for all available HFRs were used to estimate the vector velocity field using the Optimal Interpolation (OI) method (Clary et al., 2019; Kim et al., 2007). An exponential OI kernel function was used here with a constant lengthscale of 2 km, the grid spacing, and a search area radius of 6 km. Apart from the OI method's use of the search area to estimate the vector currents, no other interpolation of the vector velocities is used to fill potential gaps in HFR coverage or otherwise alter the data. Recent work by Clary et al. (2019) has shown the OI method to be superior to the more standard least squares methods for computing WNS and,

Table 2
In Situ Observations

Mooring	Lon	Lat	Water Depth	Data type	Instrument	Depths (m)	Sample Rate	Bin(m)
July-November 2018 and July-November 2019								
Center surface	41.0669°N	70.4828°W	40 m	winds, Tair, P, RH, Temp/Cond	WXT520 SBE37s	2 m amsl[a] 0.6,4,6.5,10, 15,20,30,35	10 min 2 min	0.252
Center subsurface	41.0669°N	70.4828°W	40 m	Currents currents	Nortek Signature 1000 RDI Workhorse 600	8 9	2048 pings @4 Hz every 20 min 3-ping ens every 3 s	
West	41.1185°N	70.5812°W	40 m	Temp/Cond	SBE37s	0.6,4,6.5,10, 15,20,30	2 min	
South	40.9881°N	70.5455°W	50 m	Temp/Cond	SBE37s	0.6,4,6.5,10, 15,20,30	2 min	
October-December 2020								
Center surface	41.0706°N	70.8177°W	40 m	winds, Tair, P, RH, Temp/Cond	WXT520 SBE37s	2 m amsl[a] 0.6,4,6.5, 10,20	10 min 2 min	0.25
Center subsurface	41.0706°N	70.8177°W	40 m	currents	Nortek Signature 1000	8	2048 pings @4 Hz every 20 min	

[a]above mean sea level.

additionally, spectral fluxes. For the velocity data along each analysis line, vector surface currents were processed using T_Tide (Pawlowicz et al., 2002) to remove an estimate of the six dominant tidal constituents with periods less than 2 days (M_2, S_2, N_2, K_1, O_1, and Q_1), and limited to times when the longest, gap free, transects covered greater than 70% of the analysis line; or 14,000–15,000 individual transects per line. De-tided velocities were rotated into an along- and across-line coordinate system following the local orientation of the isobaths.

For both velocity as well as temperature or salinity transects from the Wave Gliders or AVHRR (shown in Figure 2), a single wavenumber periodogram was estimated for each isolated transect, with the mean removed and a hanning window applied. Individual estimates were renormalized for the reduction in power due to the hanning window. The effects of potentially non-uniform data series lengths were mitigated by collecting the individual periodogram results, with no interpolation, and averaging over the time period of interest within discrete wavenumber bins. For comparison, a synthetic transect with a $k^{-5/3}$ red noise spectrum and a standard deviation matching the observed HFR rms differences against in situ ADCPs of 7 cm s^{-1}, was created for each velocity data series and masked with the same data gaps as the velocity observations. This noise series illustrates the impact of data gaps on the spectral results and serves as a noise floor for the ensemble averaged results. Error bounds for time-averaged spectral results were estimated using χ^2 95% and 5% confidence intervals for the sample size within each wavenumber bin for each temporal average of the spectral estimates. A representative example of the confidence interval is shown in Figure 7.

3.3. Spectral Kinetic Energy Fluxes

Within the spectral kinetic energy budget, written following Scott and Wang (2005) as

$$\frac{\partial}{\partial t} E(k) + \Pi(k) = -D(k) + F(k), \tag{1}$$

the first two terms, the time rate of change of kinetic energy and spectral kinetic energy flux Π, balance the energy dissipation (D) and energy inputs via forcings (F) on a scale-by-scale basis. Here, the spectral kinetic energy flux

$$\Pi(k) = \langle \mathbf{u}_< \cdot \left(\mathbf{u}_< \cdot \nabla \mathbf{u}_> \right) \rangle + \langle \mathbf{u}_< \cdot \left(\mathbf{u}_> \cdot \nabla \mathbf{u}_> \right) \rangle \tag{2}$$

can be estimated using the low-pass filtered, $\mathbf{u}_<$, and high-pass filtered, $\mathbf{u}_>$, currents in the wave number domain, where

$$\mathbf{u}_< = \sum_{|\mathbf{k}|<k} \hat{\mathbf{u}}(\mathbf{k}) e^{i\mathbf{k}\mathbf{x}} \tag{3}$$

$$\mathbf{u}_> = \sum_{|\mathbf{k}|\geq k} \hat{\mathbf{u}}(\mathbf{k}) e^{i\mathbf{k}\mathbf{x}} \tag{4}$$

and $\hat{\mathbf{u}}$ are the Fourier coefficients of the currents $\mathbf{u}$. Following Scott and Wang (2005) and Arbic et al. (2013), as well as more recent HFR-focused efforts (Clary et al., 2019; Soh & Kim, 2018; Yoo and Kim, 2018), spectral KE fluxes were estimated here for the more well-sampled eastern domain. However, because of data availability at the longest scales, our approach uses data from the eastern along- and across-shelf lines shown in Figure 3, instead of a square domain, to estimate locally relevant along-shelf gradients of velocity using the along-shelf lines, and across-shelf gradients using the across-shelf lines. Summations of the real and imaginary Fourier coefficients of the velocities and their derivatives along the transects were evaluated for wavenumbers both higher and lower than each wavenumber (k) following (3) and (4), to estimate the wavenumber-dependent KE flux, $\Pi(k)$, following (2) for a moving 2-day time window.

This approach, using 1D along- and across-shelf lines to estimate 2D KE fluxes, is an approximation to the two-dimensional flux described by Scott and Wang (2005) or Arbic et al. (2013), and was compared to estimates of the spectral flux utilizing 2D FFTs of a smaller, square domain within the eastern area for consistency. The results shown below, using the along- and across-shelf line approximation, are similar to results from the 2D FFTs (not shown here), but allow a greater interpretation of the results due to the higher data return and lower uncertainty levels. The direct 2D approach suffers from reduce data return due to the more stringent data needs of the 2D FFT and the gappy nature of HFR observations, leading to significantly higher uncertainties for temporal averages of KE fluxes. Use of the curved along-shelf line within this calculation did not appear to effect the results, likely as the scale of the bathymetric change was longer than the internal Rossby radius, suggesting that the flow field is locally "along-shelf uniform."

As for its interpretation, the flux of kinetic energy within a system moves energy from the scales at which it is input to higher wavenumbers –smaller lengthscales– where it is dissipated via horizontal or isotropic stirring, and to lower wavenumbers –larger lengthscales– where it can influence the low frequency or mean structure present. The spectral KE flux should have a characteristic shape, with positive values at higher wavenumbers which indicates a transfer of energy to smaller scales, and negative values at lower wavenumbers which indicates a transfer of energy from smaller scales to larger scales. Thus, the zero crossing of the spectral KE flux suggests the lengthscale at which kinetic energy flux transitions from up-scale to down-scale transfer in the ocean and, potentially, the lengthscales at which instabilities input energy into the system (Soh & Kim, 2018). Given this dynamical underpinning, estimates of the KE fluxes from HFR-based surface currents can be a critical indicator of horizontal energy exchange and stirring at the ocean's surface.

4. Results

4.1. Hydrographic Variability

Seasonal hydrographic conditions over the NES progress from stratified with shallow mixed layer depths in July and August to weakly stratified and cooling during November and December. Illustrated best via changes in surface and bottom water temperatures (Figure 4a), surface temperatures increased to up to 24–25°C in August before decreasing through the fall and winter. Bottom temperatures increased over the season, likely due to vertical mixing driven by tides (Lentz, 2017), until cooling began in October. The vertical structure of the water column at the central mooring, shown in Figure 4b during 2018, illustrates the temporal evolution of vertical stratification. Mixed layer depths, defined as the depth of a 0.1 kg/m^3 increase from the density at the surface, generally varied between 4 and 8 m in summer, before undergoing large, rapid, full-water column shifts during September and October. The water column was weakly stratified by the beginning of October in all years. Both across-shelf and vertical gradients in density (shown in Figure 4c for the central mooring location in 2018 and 2019 only) were large during summer, up to -1×10^{-6} and 4×10^{-3} kg m^{-3} respectively, but were reduced in magnitude in fall, and near zero in winter. Across-shelf density gradients at the surface were generally negative (denser surface waters onshore) throughout summer, but weaker and more variable in fall.
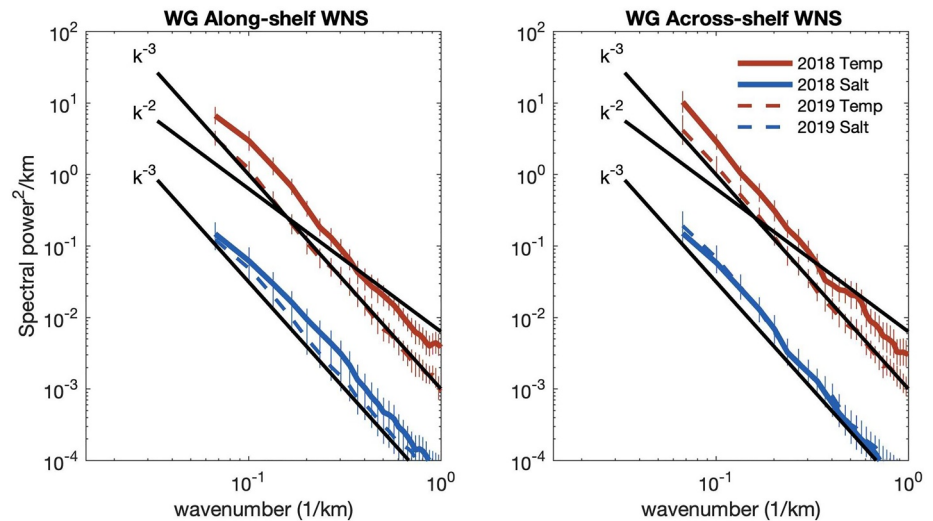
Figure 5. Time average of the approximately daily sampled scalar WNS for surface temperature (red, upper curves, in $C^{\circ 2}$) and salinity (blue, lower curves, in absolute salinity Sa^2) along the eastern (left) along- and (right) across-shelf transect lines of the Liquid Robotics Wave Gliders.

Surface waters over the wider area sampled by the Wave Gliders had variable density gradients that were predominantly temperature-dominated in June and July, as suggested by satellite SSTs (i.e., Figure 1), before becoming more salinity-dominated in late August (not shown here). Surface temperature and salinity WNS from the repeat Wave Glider transects of the along-shelf and across-shelf lines, collected within the eastern domain during summer and fall of 2018 and 2019 reveal the magnitude and structure of the scalar variance by lengthscale. For both temperature and salinity, a constant k^{-3} spectral slope was observed for along- and across-shelf lines during both years, from lengthscales of 17–1 km (Figure 5). While 2018 temperature WNS had higher overall energy levels than temperature spectra from 2019, no significant difference was found for salinity. The along- and across-shelf Wave Glider results were qualitatively similar to the mean spectral slopes from AVHRR SSTs (Figure 2) as well the east and west "along-isopycnal" transects (not shown here) suggesting the results shown here are representative of the spice variance in the region.

4.2. Mean and Eddy Kinetic Energy

Surface currents over the NES are predominantly wind forced (Dickey & Williams, 2001), with winds generally out of the southwest during July and August, but switch to be more variable in direction during November and December (Kirincich & Lentz, 2017). Wind speeds are slightly larger in November-December than in July-August with the transition between marked by shorter time-scale synoptic events with potentially high winds (i.e., fall storms as shown in Figure 6a for 2019). Both the mean kinetic energy (MKE–calculated from the vector spatial mean of the velocity along each line) and eddy kinetic energy (EKE–anomalies from the spatial mean), aggregated over the analysis lines shown in Figure 3, exhibited event-scale variability on time scales of the wind itself (3–10 days, Figure 6). During July and August, timeseries of MKE in both the eastern and western areas were significantly correlated with the wind speed in all years (CC = 0.5–0.7 at zero lag), but generally had a higher negative correlation to the across-shelf (northeastward in the eastern half of the study area) winds, with correlations (CC = −0.7 to −0.8). Events in MKE were also related to changes in the across-shelf surface density gradient (Figure 4: CC = 0.67 and 0.75 for 2018 and 2019). During periods of weakly stratified or cooling conditions that occurred after mid-October, the correlation of MKE with wind speed increased in all years (CC ~0.75). After October, large values of MKE were generally associated with negative across-shelf winds (toward the southwest in the eastern half of the study area), with winds in the opposite direction associated with a much weaker MKE response (not shown here).

On seasonal timescales, EKE estimated along the transect lines tended to decrease over time, with larger amplitude fluctuations occurring during July and August. Here, EKE (Figures 6b and 6c: red lines) was generally small in relation to MKE magnitudes during wind events and uncorrelated with either the MKE or the surface winds
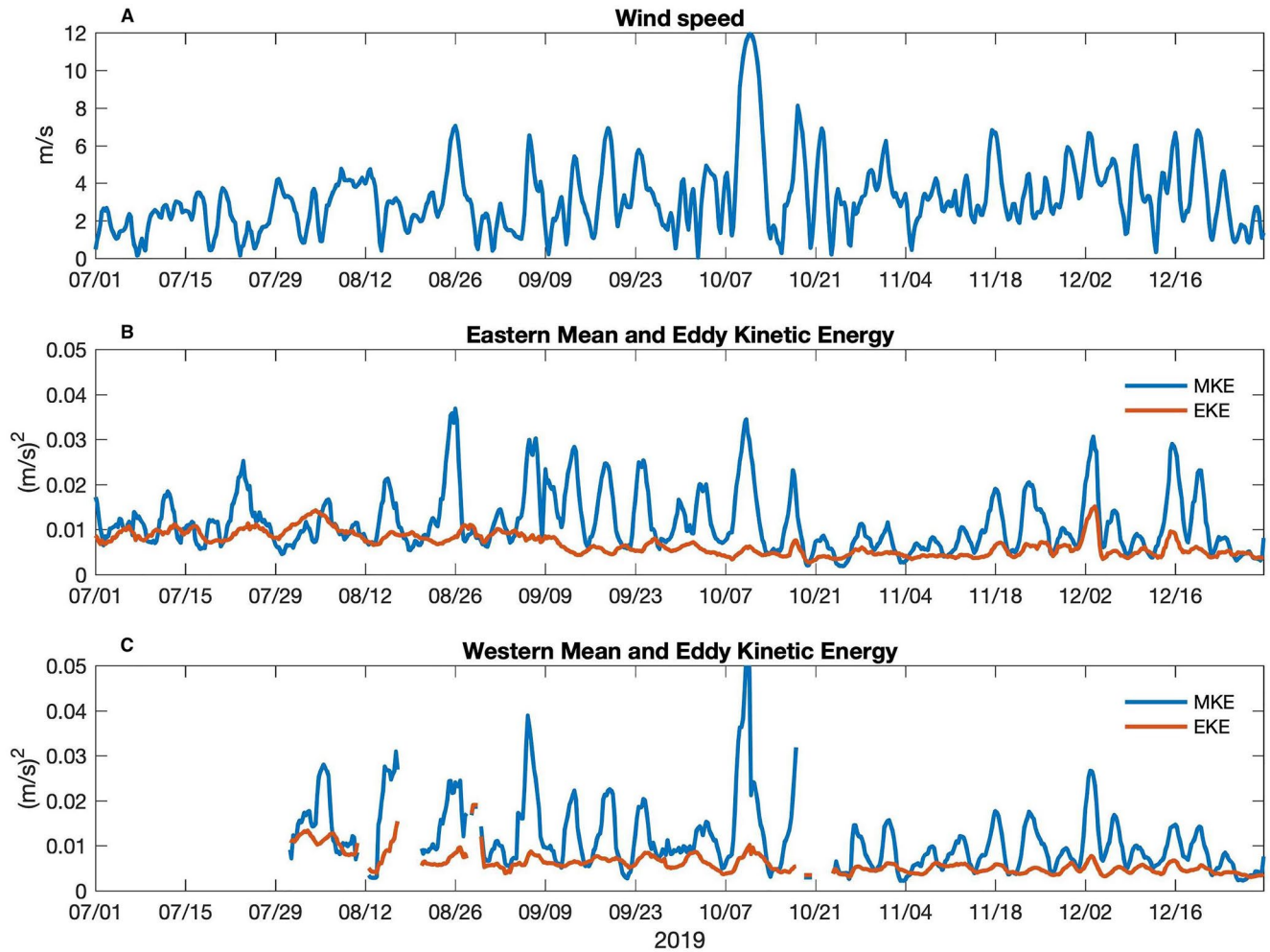
Figure 6. (top) 2019 along- and across-shelf winds with (middle) Eastern and (bottom) Western components of the along-shelf line-averaged mean kinetic energy (MKE) and eddy kinetic energy (EKE). Data from all along-shelf lines were averaged together to produce the area-averaged MKE and EKEs.

(Figure 6). In November-December, EKE was weakly correlated to the local wind speed. Thus, while the MKE, or the spatial mean of the surface velocity fields, was significantly correlated with local winds, true for any of the analysis lines used here as well as regionally (Kirincich & Lentz, 2017), anomalies from the spatial mean and their energy levels –represented by the EKE– were generally not related to local winds nor horizontal density gradients.

4.3. Kinetic Energy Wavenumber Spectra: Seasonal and Regional Variability

By definition, the transect-averaged EKE described above is equal to the integral of the wavenumber spectrum (WNS) of surface velocity along the transect. While the transect-averaged EKE describes the temporal variability of the velocity variance at the surface, integrated over the resolved spatial scales (Figure 6), the WNS of the EKE reveal the lengthscales that dominate EKE and the cascade of energy. Averaging the individual periodogram results within discrete wavenumber bins for stratified (July-September, defined here as summer), and weakly stratified (October-December, defined here as winter) periods, seasonal mean WNS for each series of transect lines were estimated (Figure 7).

Seasonal mean WNS for the along-shelf and eastern across-shelf lines at higher wavenumbers were generally linear in log space, similar to a $k^{-5/3}$ spectral slope in 2019 (thick lines), but shallower than $k^{-5/3}$ in other years. At wavenumbers less than 0.03 km^{-1} (33 km lengthscales), spectral slopes decreased toward k^{-1}. Across-shelf WNS
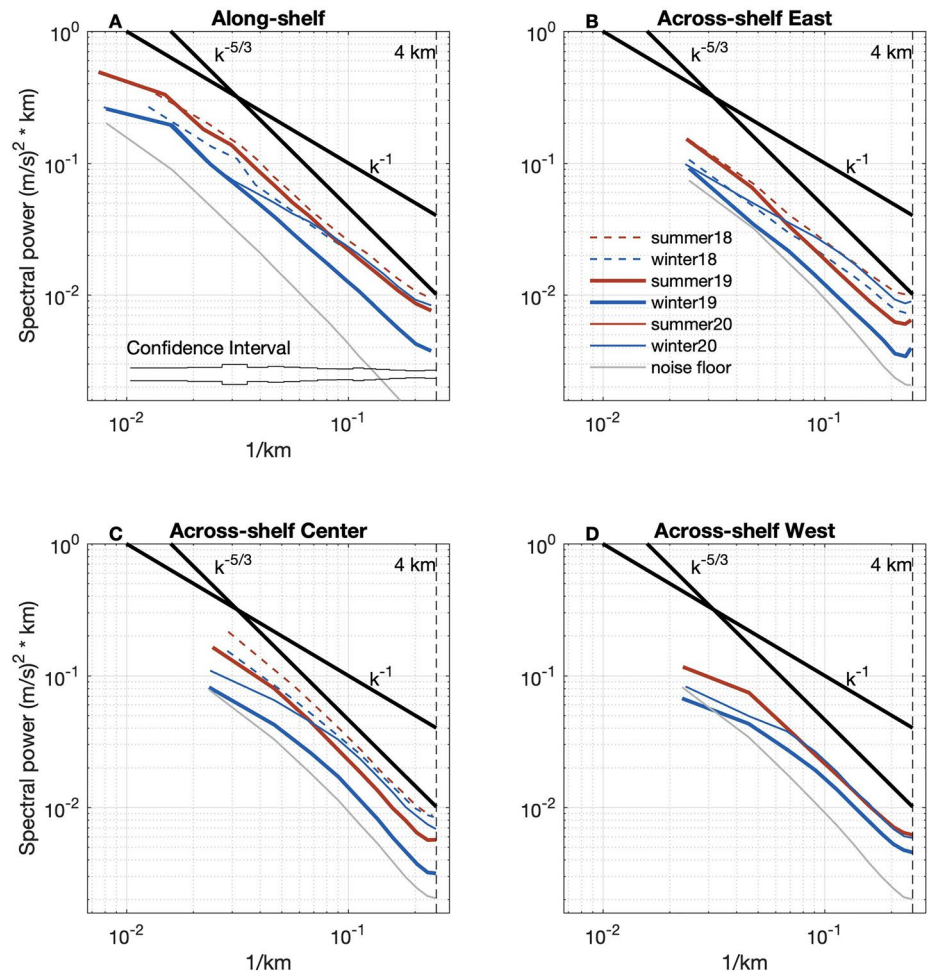
Figure 7. Seasonally averaged EKE wavenumber spectra (WNS) for the (a) Along-shelf and across-shelf (b) East, (c) center, and (d) West analysis lines. Averaged spectra for (red) summer and (blue) winter, as defined in the text, for (dashed lines) 2018, (thick lines) 2019, and (thin lines) 2020 are shown in each panel, with the similarly averaged $k^{-5/3}$ noise spectrum (gray). A representative example of the spectral confidence intervals for the wavenumber bin averages is shown in (a), using the χ^2 95% and 5% intervals for the independent degrees of freedom (N^*) in each wavenumber bin. Thick black lines show sample $k^{-5/3}$ and k^{-1} spectral slopes while the thin vertical dashed line denotes the 4 km effective resolution of the radars.

slopes in the central and western area were also consistent with a $k^{-5/3}$ spectral slope at high wavenumbers, but flattened at low wavenumbers (larger lengthscales).

EKE was notably higher at low wavenumbers in summer compared to winter in all years. For example, along-shelf summer energies were double that observed in winter at wavenumbers greater than 0.03 km^{-1} (33 km lengthscales), but the same magnitude at higher wavenumbers in both 2018 and 2020 (Figure 7a). For all lines, while the absolute energy levels at high wavenumbers (0.2–0.067 km^{-1} or 5–15 km) were quite variable both between seasons and years, the spectral slopes were more uniform. In this range, seasonal differences appeared to be just as large as differences between subsequent years. Overall energy levels were lowest for the eastern across-shelf lines and the western across-shelf lines at low wavenumbers, where seasonal averages approach the noise spectrum. Comparing years, the winter 2020 results were notable along all lines as the energy levels were the least consistent with a constant slope, with much of the change in slope occurring near 0.05 km^{-1} (20 km) as energy levels at higher wavenumbers (0.2–0.067 km^{-1} or 5–15 km) were higher in 2020 than most other years. Energy levels were the lowest during winter 2019 (Figure 7: blue thick lines), where spectral slopes were the most similar to a $k^{-5/3}$ slope over the largest range in wavenumber.

The ratio of the across-track to along-track KE WNS reveals the orientation of the eddy structures (i.e., the aniso-trophy of the velocity field) contributing to the total EKE (see Rocha et al., 2016, for details). During summer
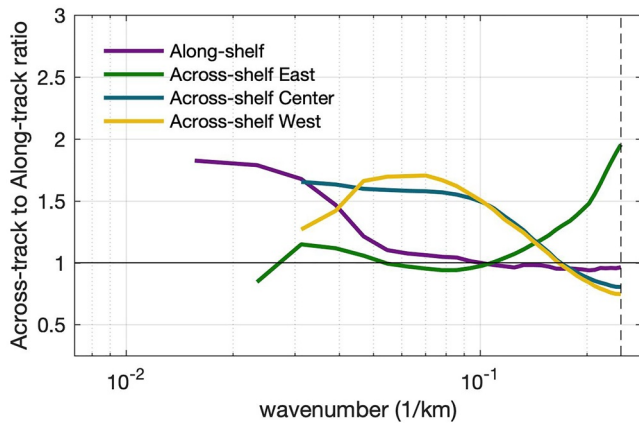
Figure 8. The ratio of across-track to along-track velocity spectra for the (purple) along-shelf transect, extending to 0.017 km^{-1} (60 km) and the (green) eastern, (blue) central, and (yellow) western across-shelf transects during summer 2019. These results are representative of the ratios during the remainder of the sampled periods.

2019, which was representative of the full data set, the along-shelf line had an across to along-track ratio of ~1 for wavenumbers greater than 0.5 km^{-1} (20 km), but higher values at lower wavenumbers. Along the western and central across-shelf transects, the ratio was greater than one at scales less than 0.1 km^{-1} (10 km), suggesting that the largest flow structures contributing to the EKE at those scales were the eastward (across-transect) velocities. However, the ratio decreased to near 1 at 0.2 km^{-1} (5 km), suggesting that the flow field was less polarized at higher wavenumbers in this region. In contrast, the eastern across-shelf line's currents were similar in magnitude, with a ratio near one, for all but the smallest scales. At the longest scales measured here, possible only along the along-shelf transects, across-shelf currents were more energetic, a somewhat unexpected result.

4.4. Spectral Kinetic Energy Fluxes

As described previously (in Section 3.3 and Scott & Wang, 2005; Arbic et al., 2013; Soh & Kim, 2018), spectral KE fluxes should have a characteristic shape with wavenumber, with positive fluxes at greater wavenumbers, indicating a transfer of energy to smaller scales, and negative values at smaller wavenumbers, indicating a transfer of energy from smaller scales to larger scales. At lengthscales where $\Pi(k)$ has a positive slope, the spectral flux is divergent and thus there is a source of kinetic energy at these scales (Scott & Wang, 2005). In contrast, the spectral flux is convergent where $\Pi(k)$ has negative slopes, implying a sink of kinetic energy at these scales. At the zero crossing of $\Pi(k)$, which occurs where $\Pi(k)$ has a positive slope, energy is flowing to larger (smaller) scales at wave numbers less than (greater than) the wavenumber of the zero crossing. Thus, the zero crossing of the spectral KE flux signifies the lengthscale at which the source of kinetic energy to the system changes from an inverse to a forward cascade.

Averaged over the eastern portion of the domain using both the along- and across-shelf transects centered at the 2018–2019 mooring location (41.0669°N, 70.4828°W, Figure 3) and in time for each month sampled across the three observational periods, the mean KE spectral flux was estimated between wavenumbers of 0.25–0.025 km^{-1} (4–40 km scales; Figure 9). The longest scale sampled was limited by the length of the across-shelf analysis lines. KE flux results were generally either slightly greater than, or not significantly different from, zero at wavenumbers higher than 0.07 km^{-1} (15 km), but varied significantly at lower wavenumbers. Low wavenumber KE fluxes were negative in July at wavenumbers below 0.055 km^{-1} (~18 km), reaching mean values up to -3.5×10^{-8} m^2 s^{-3}. Negative values at low wavenumbers decreased in August, were variable and generally not different than zero for September and October, and became positive for both November and December (Figure 9). Both the mean results in July and August exhibited a zero crossing from negative to positive values at lengthscales near 18 km, while September and October tended to have zero crossings at slightly longer lengthscales. No notable zero crossings of the mean KE fluxes occurred in November and December, with only small positive mean values observed.

Summarizing these results, during summer (July - August) at scales greater than 18 km the monthly mean EKE flux is to larger scales, while at scales less than 18 km the EKE flux is toward smaller scales. However, in winter (Nov - Dec) the EKE flux is toward smaller scales for all the resolved scales suggesting the transition occurs at scales longer than 40 km.

The variability of the KE fluxes on shorter, synoptic timescales can be examined from mean KE fluxes estimated over a moving 2-day time window (Figure 10). Error estimates for the 2-day mean fluxes, using the ADCP to HFR comparisons for an estimate of the velocity error, ~7 cm s^{-1}, and the number of independent realizations within each average, give an error bound of 0.5×10^{-8} m^2 s^{-3}. Estimated fluxes less than this error bound were considered to be not significantly different than zero and thus are not shown here (Figure 10). Within the significant 2-day averaged KE fluxes, large periods of negative fluxes occur at low wavenumbers during summer in both 2018 and 2019 (e.g., 7/15 in 2018 or 2019 in Figure 10), but are interspersed with periods of weak or positive fluxes at low wavenumbers. Fluxes at higher wavenumbers are generally less than the error estimate or positive. Between September and October, the occurrence of large negative values at low wave numbers paired with positive values at higher wavenumbers stops, and KE fluxes are near-zero with frequent positive pluses over
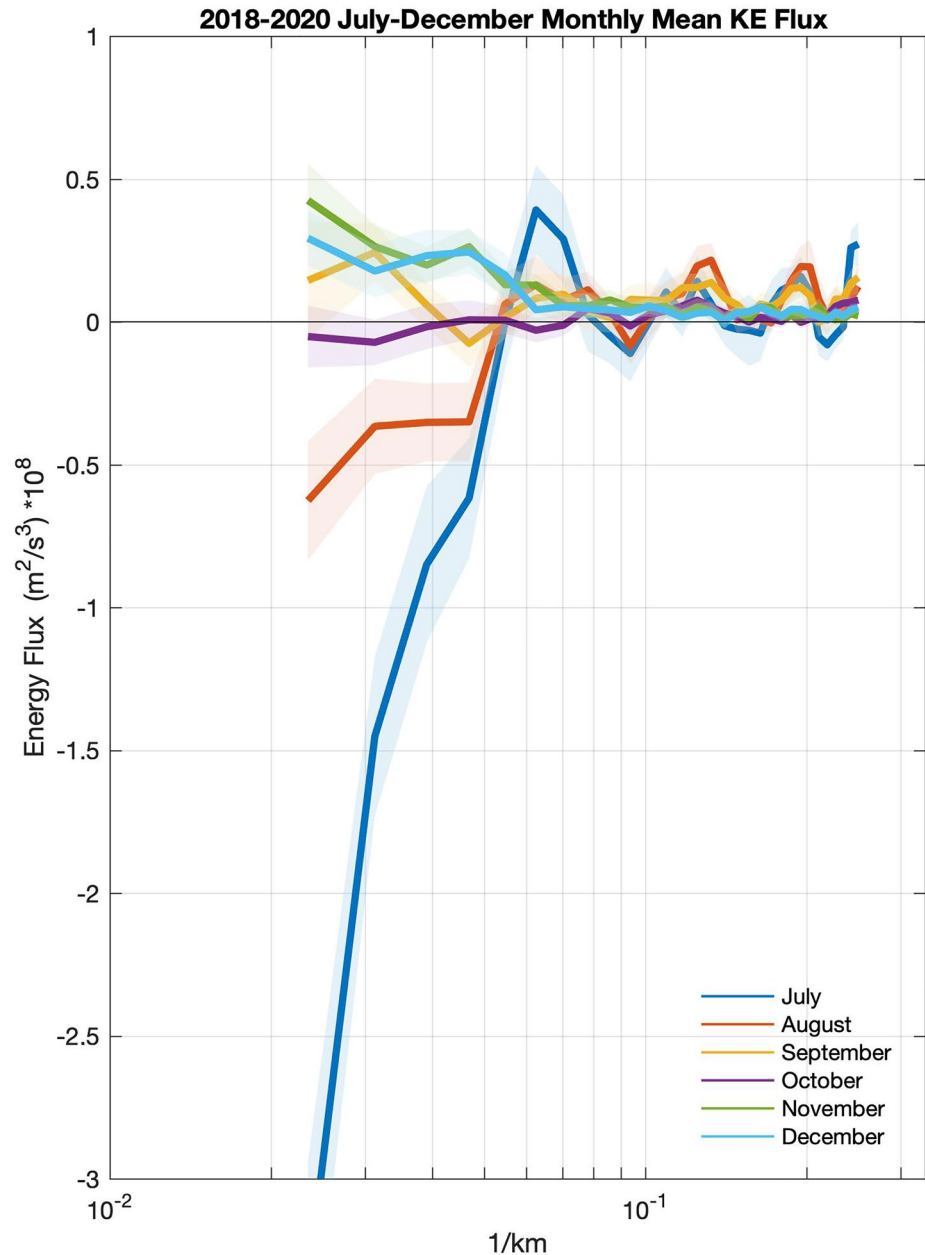
Figure 9. Monthly averaged spectral KE fluxes for the eastern half of the HFR coverage area using the along- and across-shelf lines from all 3 years, when available. Standard error bounds of the monthly means are shown for each month.

a large range of wavenumbers (scales of 40 to 10 km or higher) or, more rarely, all-negative during winter months (Figure 10).

The correspondence of the synoptic variability of KE fluxes to winds or stratification was evaluated by comparing the 2-day windowed timeseries of KE flux at both low wavenumbers and high wavenumbers to the observed winds and stratification. KE fluxes measured within two wavenumber ranges, from 30 to 20 km and 13-10 km, were compared with conditions present in July-August, September-October, and November-December separately. The KE fluxes in these wavenumber bands were chosen instead of an estimate of the lengthscale of the zero crossing as they were on opposite sides of the mean zero crossing in KE flux observed during summer and form a continuous timeseries, whereas the transition scale would be undefined when no zero crossing existed (Figure 10).
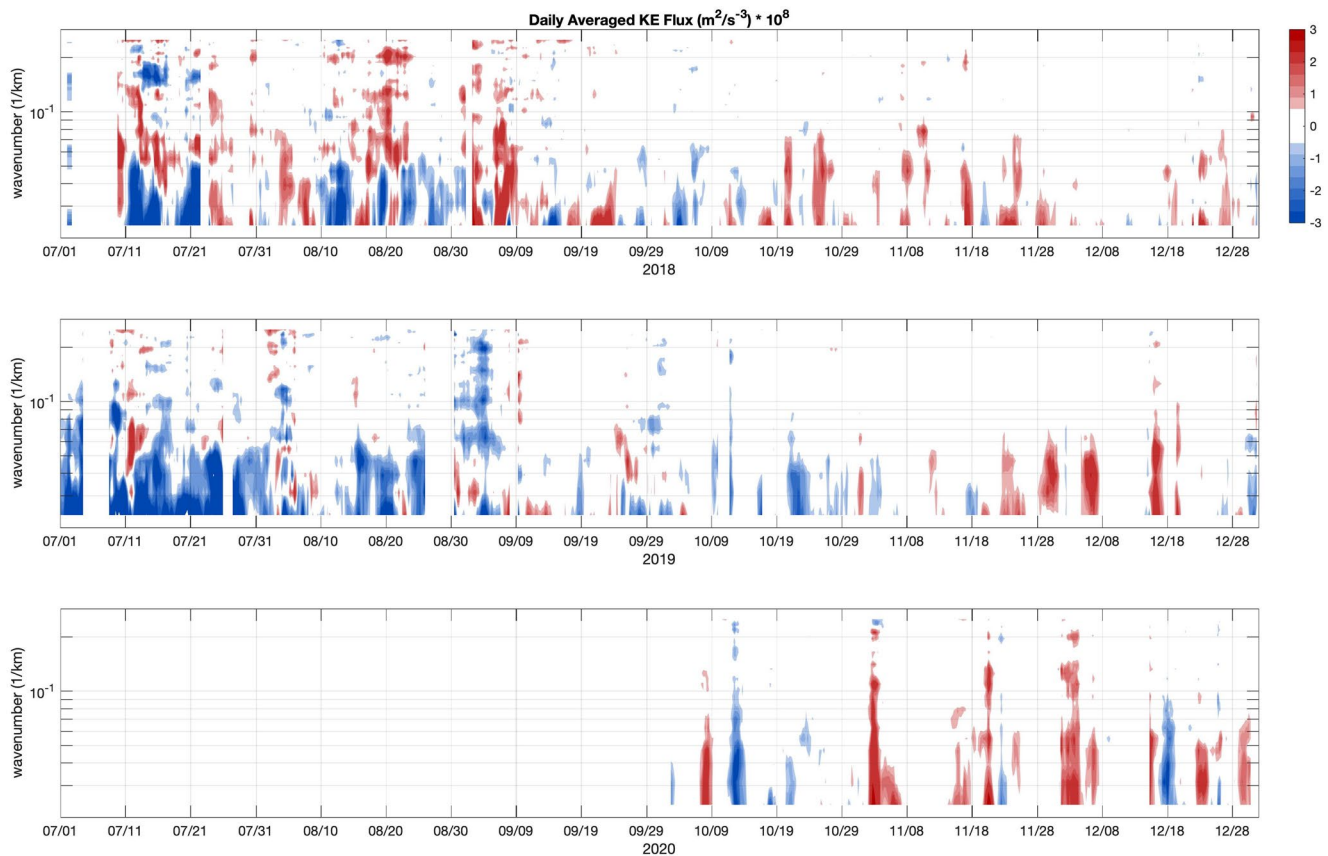
Figure 10. Moving 2-day averaged spectral KE fluxes for the eastern half of the HFR coverage area using the along- and across-shelf lines for all years, when available. Based on the error estimates for the 2-day means, fluxes less than 0.5×10^{-8} m^2 s^{-3} are likely not significantly different than zero and not shown.

In summer (July-August), low wavenumbers or long scales were positively correlated with the along-shelf winds (2018: CC = 0.53) or the wind speed itself (2019: CC = 0.45). In both years, a weak relationship between the KE flux at low wavenumbers and the vertical stratification also existed (CC = 0.37). In fall (September-October), the low wavenumber KE fluxes were most significantly related to along-shelf winds (CC = 0.55,0.67 in 2019, 2020), and more weakly to either vertical or horizontal density gradients (CC ~0.4–0.5) for both low and high wave numbers. In winter months (November-December), both flux timeseries were positively correlated with the along-shelf winds (CC > 0.6) and to each other, suggesting that the energy in both ranges of scales co-vary with magnitudes related to the wind forcing.

5. Discussion

HFR-based measurements of surface currents provide a vastly larger sample size, compared to satellite-based SST images or in situ observations, for estimating the statistics of wavenumber spectra, allowing a detailed examination of horizontal stirring over the shelf, its seasonal, regional, and scale-dependent variability, and its relationship to mean kinetic energy, winds, and stratification. Applied to the unique HFR system described here, analysis of the KE WNS provides a window into the characteristics and drivers of lateral stirring and exchange over the NES. While the MKE of surface currents was directly related to wind forcing on synoptic timescales, EKE–defined as the anomaly from the spatial mean–was generally not. Inter-annual variability in the seasonally averaged EKE WNS (Figure 7) was likely driven in part by variability in the seasonally averaged wind field. For example, winter winds in 2020 were notably more intense than in 2018 and especially 2019, likely causing the spread of WNS observed. Regional differences in both the magnitude of EKE and its spectral shape also existed over relatively short along-shelf spatial scales. In the west, the effects of nearby topography were likely a constraint to the flow field, but this alone does not explain the seasonal progression to flatter WNS at longer

scales in winter. In the east, the reduced energy levels found in the across-shelf direction were likely a function of the along-shelf polarization of currents.

5.1. Comparisons to Previous Estimates

Existing model and observational estimates of the energy cascade in coastal waters differ both from each other and from the results shown above. Model estimates of the energy cascade in coastal regions suggest relatively flat horizontal spectra in tracer and EKE fields at the scales at which energy is injected into the ocean (Capet et al., 2008a), and $k^{-5/3}$ or k^{-2} spectral roll-offs at higher wavenumbers, has been seen in the open ocean (Callies & Ferrari, 2013; Rocha et al., 2016). Importantly, Capet et al. (2008a) also used the change in spectral slope at the highest wavenumber, from $k^{-5/3}$ or k^{-2} to higher slopes, as evidence of the wavenumber limitation of the model itself. Prior HFR-based analyses of spectral slopes (Soh & Kim, 2018; Yoo and Kim, 2018) from coastal areas deeper than that studied here, but similar to the conditions of (Capet et al., 2008a), found a $k^{-5/3}$ roll-off at the very longest scales, a sharper k^{-3} roll-off at scales smaller than 10 km, and a flattening of spectra as scales approached ∼2 km, corresponding to the Nyquist wavenumber.

The results shown here support the model spectral estimates given by Capet et al. (2008a) in that their slopes were near $k^{-5/3}$ at scales that were smaller than the domain size and potentially driven by internal ocean dynamics, but were flatter (more similar to k^{-1}) at longer scales. No second or additional roll-off was found at the highest wavenumbers sampled. However, we note that spectral estimates at both the low- and high-wavenumber ends of a discrete spectrum can be biased by the preparation of the data itself, either by pre-whitening techniques that tend to flatten energy at the lowest wavenumbers observed (Priestley, 1981) or, specific to HFR-based velocity estimates, by the methodology used to estimate vector velocities from the radial currents. Detailed tests of the latter effect by Clary et al. (2019) found that the OI method had a minimal impact on WNS and KE flux estimates compared to unweighted least squares estimates that used the same search area. However, the OI method's results at high wavenumbers are also dependent on both the lengthscale and search radius chosen, as a larger OI kernel lengthscale increases the relative weight of distant radial data on the local average, and a larger search area effectively allows greater interpolation over missing data values. In tests performed here, larger values of either the kernel lengthscale or the search radius–relative to the native resolution of the radar–have the effect of depressing spectral energies at high wavenumbers–increasing the relative slope–but flattening spectra at the Nyquist. Compared to Soh and Kim (2018) or Yoo and Kim (2018), we use a coarser grid spacing and smaller lengthscale and search areas relative to the native resolution of the radar to limit this potential effect. However, the flattening of the wavenumber spectra seen at 4 km (e.g., Figure 7a) was likely a result of this observational bias nonetheless.

Yoo and Kim (2018) suggest that submesoscale processes in their study region, the South Korean Shelf, were maintained by baroclinic instability in the mixed layer with moderate seasonality. Over the NES, seasonal mean spectral slopes were $k^{-5/3}$ or shallower for scales less than 15 km during both strongly and weakly stratified conditions. At longer scales, spectral slopes varied considerably, with regional and inter-annual variability in the slopes and energy levels larger than the seasonal differences. Seasonal mean spectral slopes were most consistent over a broad range in wavenumber for the along-shelf and eastern across-shelf lines. Only as the spatial scales were potentially limited by the shelf geometry in the west did the EKE slopes appear to vary with wavenumber in summer. Thus, it is not clear if the mean spectral slope seen in the along-shelf segment maintains a constant slope to low wavenumbers because the density front present allows a wide range of baroclinic instabilities to be generated, or simply because the along-shelf segments are more free of topographical influence.

A second interpretation of our results is that they align with sQG theories (i.e., Lapeyre & Klein, 2006) which suggest decay slopes are $k^{-5/3}$ at scales where a forward cascade is occurring, and k^{-1} at longer scales where an inverse cascade is occurring (Yoo and Kim, 2018). In this interpretation, the break in slope between $k^{-5/3}$ and k^{-1} marks the transition scale. However, the flatting of spectra at low wavenumber as the mixed layer disappears in the west is somewhat opposite that predicted by sQG theory (Callies & Ferrari, 2013)–which requires a mixed layer over constant stratification–suggesting that the change in slope is instead due to boundary controls on the flow conditions. In the east, the monthly mean KE flux results illustrate that, despite the more uniform along-shelf spectral slopes present during summer, the transition scale–the wavenumber of the zero crossing from negative fluxes to positive fluxes–was relatively short, near 18 km. The mean lengthscale of energy flux transition moved to lower wavenumbers (longer scales) as the water column became weakly stratified.

Briefly addressing the observed tracer variance observations, temperature and salinity observations from repeat transects at the surface, as well as satellite snapshots (Figure 2) show a k^{-3} roll-off at lengthscales smaller than ~16 km with seasonality in the overall energy level but not in the slope itself. Numerous works on tracer variance spectra (summarized by Spiro Jaeger et al., 2020) have reported a range of spectral slopes at scales smaller than 10 km, with only a few estimates having sharper k^{-3} slopes. Sharper, more negative, slopes in tracer variance spectra imply more rapid stirring of waters and an intense cascade of energy from larger scales (Callies & Ferrari, 2013).

5.2. Synoptic Variability and Its Drivers

EKE WNS and KE fluxes were more strongly related to the wind forcing at synoptic timescales than the spatially integrated EKE. EKE WNS varied dramatically over both synoptic and intra-seasonal timescales, and were often spatially consistent over wide areas (not shown here). KE fluxes at low wavenumbers (long scales) were consistently related to local winds, and along-shelf winds in particular. Based on this correspondence, we suggest that the winds, while not often directly related to the magnitude of EKE –in contrast to MKE– or the spectral rolloff of energy, heavily influenced the scales at which energy was added to the coastal ocean. While seasonal changes in the KE flux transition scale mirror those in stratification, the transition scale is clearly "wind-driven" on synoptic timescales (Figure 10).

A related, curious result of the present work was the significant relationship between the along-shelf component of the wind (as distinct from the scalar wind speed) and the low-wavenumber KE flux in all periods. Previous results using idealized, eddy-resolving numerical models have shown the direction and intensity of wind forcing along a front can contribute an Ekman buoyancy flux. Up-front winds lead to rapid re-stratification of a frontal feature (Mahadevan et al., 2012), while in the presence of either down-front winds or a background along-shelf flow, the Ekman layer transport acts to reinforce the front (Thomas & Lee, 2005). With dense water on its right, or inshore side, negative along-shelf (westward) winds over the NES would be equivalent to "up-front winds" (Mahadevan & Tandon, 2006), both energizing the regional MKE and pushing lighter waters to the northeast (across-shelf), re-stratifying an existing front, and potentially decreasing the mixed-layer depth. With a positive correlation between KE flux at low wavenumbers and the along-shelf wind, negative along-shelf – or westward – winds occur with negative KE fluxes, and appear with a transition scale that is within the array's measured range (4–40 km). The Ekman transport due to positive along-shelf winds, which would reinforce the front, is associated here with positive KE flux at low wavenumbers and thus a transition scale that is longer than 40 km.

The along-shelf WNS results, with consistent spectral slopes over a wide range of wavenumbers, parallel both open ocean results that examine submesoscale energy cascades (e.g., Callies & Ferrari, 2013) as well as coastal-focused efforts examining instabilities of idealized tidal mixing fronts (i.e., Brink & Seo, 2015). Given its proximity to the study area, the tidal mixing front over Nantucket Shoals (to the east in Figure 1) was a key source of horizontal buoyancy gradients to the study area during summer, but observed density gradients were small during winter. While the presence of buoyancy gradients should, according to theory, dictate the characteristics of the instabilities created, the results shown here suggest that local winds drove the synoptic variability of EKE in all seasons as, on synoptic timescales, the magnitude and sign of the KE flux were generally unrelated to local density gradients. That local winds appear to dominate the scales of KE fluxes and likely the dominant spatial scales of the resulting flows, is a critical result. In most model-based studies of frontal instabilities (i.e., Brink & Seo, 2015), the frontal dynamics require 10s of days with constant or sinusoidal wind forcing to produce results that are similar to that shown here. The features in our observations appear to evolve over timescales that are an order of magnitude shorter. Further examination of the interplay of the spatial scales of buoyancy gradients and the spatial scales of the winds themselves on controlling the local dynamics present are required to better understand the interaction of wind forcing on the dominant lengthscales.

5.3. Implications For Lateral Stirring

The results shown here are representative of the NES, but also reveal key characteristics of lateral stirring of the larger MAB. A comparison of the AVHRR SST results from the stratified portions of the study period to a wider period of 8 years (spanning 2013–2020) found that spectral estimates during both the 2018 and 2019 field periods were similar to the 8-year average in all periods, with only small changes in energy levels, but no significant

change in the spectral shape. These comparisons illustrate that the general trend of steeper roll-offs in tracer variance at scales less than 15–20 km was a consistent feature of the NES, suggesting that intense lateral mixing processes at those scales are routinely present. The results shown here are also likely representative of the MAB more generally, despite being located proximate to Nantucket Shoals, one of the larger sources of surface density variance in the region. As can be readily seen in individual SST images (i.e., Figure 1), the sharper frontal features found in the east, adjacent to the shoals, degrade toward the west. Yet little variation exists among the EKE WNS at smaller scales, or any scale during the summer stratified period, as shown by the across-shelf line results. Thus, it is likely that other portions of the MAB, or other wide, flat shelves with sources of horizontal stratification, will have similar results. The potential differences between wide and narrow shelf environments can likely be seen in contrasting this work with Yoo and Kim (2018), for example.

Although the instability mechanisms might not be clear here, the regional and along- and across-shelf differences are, illustrating both the background, seasonally varying energy cascade present as well as the temporally and spatially rapid changes in the energy-containing horizontal scales that can occur relative to that cascade. However, the energy cascade represented by EKE WNS is an integrated view that contains magnitude but not phase (Armi & Flament, 1985) information about horizontal stirring and diffusion over the shelf. More work is needed to evaluate these characteristics in assimilative, realistic coastal models as well as translate these results into a spatially and temporally dependent eddy diffusivity to maximize our understanding of and ability to predict lateral stirring of the coastal ocean. Methods that observationally estimate diffusivity, such as a "lateral Thorpe-scale" derived from tracer variance (Klymak et al., 2015) or the spatially integrated EKE itself (Brink, 2012), are both dependent on an assumed timescale. Recent work using dynamical systems approaches (i.e., Serra et al., 2020) which focus on the structures present in the flow field that present barriers, either in time or space, to transport or exchange, give a different path toward describing space- and time-dependent stirring. We suggest that routine use of KE flux estimates to define the scales of injection and direction of energy transfer could be useful toward improving estimates of stirring over the shelf.

6. Summary

This study examined the space and time scales of EKE over the continental shelf using HFR-based observations of surface currents to estimate the wavenumber spectral properties of the surface ocean and the cascade of energy between scales. The surface current observations were placed into context using in situ timeseries of horizontal and vertical temperature and salinity gradients, local meteorological forcing, and current velocity profiles. Three distinct periods were present: a vertically stratified summer period, a fall transition to weakly stratified conditions via wind-driven mixing, and a subsequent winter period of cooling; each with characteristic wavenumber spectral properties and KE flux scale dependence. While area-averaged MKE at the surface was tightly coupled to wind forcing, EKE was not, and had reduced magnitudes in winter relative to summer in all areas. Mean EKE wavenumber spectral slopes were generally near $k^{-5/3}$, but at longer scales – lower wavenumbers – local bathymetry and topography likely flattened WNS. HFR-based estimates of spectral KE fluxes revealed a mean transition scale of energy near 18 km during stratified months, but suggested much longer scales during winter. While overall, EKE was unrelated to local winds, the up or down scale flux of kinetic energy was tied to wind events and, more weakly, to local density gradients. These results show the seasonal variability, the regional differences, and the inter-annual differences in the WNS of the EKE within the NES, but are likely representative of energy cascades over broad continental shelves similar to the MAB.

Appendix A: HFR Accuracy and Validation

HFR-based surface currents were validated against in situ velocity data from an upward-looking ADCP, deployed on the subsurface mooring, as well as mass O(10–30) drifter releases conducted during 2018 and 2019. In all years, rms differences between the east and north components of the vector surface currents at the HFR grid point nearest to the mooring location and the horizontal velocities measured by the mooring at a depth of 1.25 m below the surface were 7–8 cm/s in summer months and 5–6 cm/s in winter months for both the raw 30-min sampled HFR surface currents as well as de-tided surface currents (Table A1). Linear regression slopes for all above comparisons were near one, with correlation coefficients greater than 0.75, and typically 0.85–0.9. A 24-drifter deployment took place in the eastern half of the domain during 2018, carried out by the NSF-funded ALPHA

Table A1
HFR-ADCP[a] Comparisons

	East velocity		North velocity	
	Rmsd (cm/s)	CC	Rmsd (cm/s)	CC
2018	7.5	0.87	7.3	0.76
2019	8.5	0.83	7.1	0.78
2020	7.5	0.89	4.8	0.80

[a]1.25 m depth below surface.

project (co-I Kirincich). With most drifters spending 6 days within the radar coverage area, the RMS difference between radar and drifter velocities was 7 and 9 cm/s for the north and east velocities respectively (correlation coefficients >0.84). A smaller 10-drifter deployment was carried out in 2019 by WHOI and the USCGA, to both directly validate HFR-based surface currents as well as to test USCGA cadet-built drifter designs. Focused mostly on the western half of the radar domain and lasting more than two weeks, this release provided more than 2000 individual comparisons between velocities estimated from the radars and velocities estimated from standard surface drifters (Davis, 1985). Drifter-radar comparisons in 2019 were similar to 2018, but the wide area of sampling of the drifters revealed higher than normal errors in the east component velocities in the southwest corner of the radar coverage area (south of 41° N and west of 71° W). Likely due to an issue with the radial velocities observed by the Block Island 25 MHz radar, most of this region was excluded from the analysis presented here, which used the coverage area shown in Figure 1. As previous HFR studies (i.e., Ohlmann et al., 2007) have confirmed, a lower bound of HFR to in situ velocity comparison statistics of 3–6 cm/s exists resulting from both instrument and geophysical differences. Thus, the comparisons described above validate the high quality of the HFR observations used here.

Appendix B: Scalar Variance Data Preparation

For wavenumber spectra of the surface temperature and salinity observations collected along the Wave Glider tracks, the 2-min observations of temperature and salinity were averaged to 250-m resolution transects along each line and spectral estimates composed following the methods described above. This work follows a "fast-tow" approach, in that each transect is assumed to be a synoptic snapshot of the conditions present along the transect line, as opposed to the "slow-tow" approach often used for glider or float-based sampling of transect lines (Cole & Rudnick, 2012; Rudnick & Cole, 2011). This approach is reasonable here as: (a) the Wave Gliders generally sample the transect lines in 12–14 hr or less, and transit areas equivalent to the local tidal displacement in 1–3 hr, (b) only temperature and salinity spectra from the surface (0.3 m depth) sensors are used here, minimizing the potential effects of internal waves on WNS estimates of scalar variance at the smallest scales (Rudnick & Cole, 2011), and finally, (c) the estimated scalar WNS for both temperature and salinity had the same spectral slope as satellite-based snapshots of temperature (Figure 2), indicating that the transect sampling time of the Wave Gliders does not alter the spectral estimates.

The Wave Glider observations of the ocean's surface often encounter density gradients, particularly on the along-shelf and across-shelf oriented transects, and thus are not true estimates of along-isopycnal spice variance, which is most often examined in open-ocean studies of scalar variance (i.e., Spiro Jaeger et al., 2020). However, tests suggested that "constant-depth" estimates of the scalar WNS in the region are not significantly different from estimates made "along-isopycnal" (Cole & Rudnick, 2012; Klymak et al., 2015; Kunze et al., 2015), as transects with minimal (less than ± 0.2 kg m^{-3}) density variability – 50% of the realizations for the east and west transects – had no significant difference in spectral shape or slope from the full record.

Data Availability Statement

SST data used here are publicly available through MARACOOS (http://basin.ceoe.udel.edu/thredds/catalog/catalog.html). Processed HFR and mooring results are available via the WHOI data library, at https://doi.org/10.26025/1912/27599.

References

Aikman, F., & Ou, H. W. (1988). Shelf-slope frontal structure and cross-shelf exchange at the New England shelf-break. *Continental Shelf Research*, *8*(5–7), 687–710. https://doi.org/10.1016/0278-4343(88)90072-6

Arbic, B. K., Polzin, K. L., Scott, R. B., Richman, J. G., & Shriver, J. F. (2013). On eddy viscosity, energy cascades, and the horizontal resolution of gridded satellite altimeter products. *Journal of Physical Oceanography*, *43*(2), 283–300. https://doi.org/10.1175/JPO-D-11-0240.1

Armi, L., & Flament, P. (1985). Cautionary remarks on the spectral interpretation of turbulent flows. *Journal of Geophysical Research*, *90*(C6), 11779–11782. https://doi.org/10.1029/JC090iC06p11779

Barth, J. A. (1994). Short-wave length instabilities on coastal jets and fronts. *Journal of Geophysical Research*, *99*(C8), 16095. https://doi.org/10.1029/94JC01270

Beardsley, R., Chapman, D. C., Brink, K. H., Ramp, S., & Schlitz, R. (1985). The Nantucket shoals flux experiment (NSFE79). Part I: A basic description of the current and temperature variability. *Journal of Physical Oceanography*, *15*(6), 713–748. https://doi.org/10.1175/1520-0485(1985)015<0713:tnsfep>2.0.co;2

Beckenbach, E., & Washburn, L. (2004). Low-frequency waves in the Santa Barbara Channel observed by high-frequency radar. *Journal of Geophysical Research*, *109*(C2), C02010. https://doi.org/10.1029/2003JC001999

Bracco, A., Choi, J., Joshi, K., Luo, H., & McWilliams, J. C. (2016). Submesoscale currents in the northern Gulf of Mexico: Deep phenomena and dispersion over the continental slope. *Ocean Modelling*, *101*, 43–58. https://doi.org/10.1016/j.ocemod.2016.03.002

Brannigan, L., Marshall, D. P., Naveira-Garabato, A., & Nurser, A. J. G. (2015). The seasonal cycle of submesoscale flows. *Ocean Modelling*, *92*, 69–84. https://doi.org/10.1016/j.ocemod.2015.05.002

Brink, K. H. (2012). Baroclinic instability of an idealized tidal mixing front. *Journal of Marine Research*, *70*(4), 661–688. https://doi.org/10.1357/002224012805262716

Brink, K. H. (2015). Continental shelf baroclinic instability 1: Relaxation from upwelling or downwelling. *Journal of Physical Oceanography*, *46*(2), 551–568. https://doi.org/10.1175/JPO-D-15-0047

Brink, K. H., & Seo, H. (2015). Continental shelf baroclinic instability 2: Oscillating wind forcing. *Journal of Physical Oceanography*, *46*(2), 569–582. https://doi.org/10.1175/JPO-D-15-0048.1

Callies, J., & Ferrari, R. (2013). Interpreting energy and tracer spectra of upper-ocean turbulence in the submesoscale range (1–200 km). *Journal of Physical Oceanography*, *43*(11), 2456–2474. https://doi.org/10.1175/jpo-d-13-063.1

Callies, J., Ferrari, R., Klymak, J. M., & Gula, J. (2015). Seasonality in submesoscale turbulence. *Nature Communications*, *6*(1), 6862. https://doi.org/10.1038/ncomms7862

Capet, X., Mcwilliams, J., Molemaker, M. J., & Shchepetkin, A. F. (2008b). Mesoscale to submesoscale transition in the California current system . Part III: Energy balance and flux. *Journal of Physical Oceanography*, *38*(10), 2256–2269. https://doi.org/10.1175/2008JPO3810.1

Capet, X., McWilliams, J. C., Molemaker, M. J., & Shchepetkin, A. F. (2008a). Mesoscale to submesoscale transition in the California Current system. Part I: Flow structure, eddy flux, and observational tests. *Journal of Physical Oceanography*, *38*(1), 29–43. https://doi.org/10.1175/2007JPO3671.1

Chavanne, C., Flament, P., & Gurgel, K.-W. (2010). Interactions between a submesoscale Anticyclonic vortex and a front. *Journal of Physical Oceanography*, *40*(8), 1802–1818. https://doi.org/10.1175/2010JPO4055.1

Clary, J., Nadeau, L. P., & Chavanne, C. (2019). The effect of measurement limitations on high-frequency radar-derived spectral energy fluxes. *Journal of Atmospheric and Oceanic Technology*, *36*(11), 2139–2152. https://doi.org/10.1175/JTECH-D-18-0237.1

Cole, S. T., & Rudnick, D. L. (2012). The spatial distribution and annual cycle of upper ocean thermohaline structure. *Journal of Geophysical Research*, *117*(C2). https://doi.org/10.1029/2011JC007033

D'Asaro, E. A., Shcherbina, A. Y., Klymak, J. M., Molemaker, J., Novelli, G., Guigand, C. M., et al. (2018). Ocean convergence and the dispersion of flotsam. *Proceedings of the National Academy of Sciences of the United States of America*, *115*(6), 1162–1167. https://doi.org/10.1073/pnas.1718453115

Davis, R. E. (1985). Drifter observations of coastal surface currents during CODE: The method and descriptive view. *Journal of Geophysical Research*, *90*(C3), 4741–4755. https://doi.org/10.1029/jc090ic03p04741

Denman, K. L., & Abbott, M. R. (1994). Time scales of pattern evolution from cross-spectrum analysis of advanced very high resolution radiometer and coastal zone color scanner imagery. *Journal of Geophysical Research*, *99*(C4), 7433–7442. https://doi.org/10.1029/93JC02149

Dickey, T. D., & Williams, a. J. (2001). Interdisciplinary ocean process studies on the New England shelf. *Journal of Geophysical Research*, *106*(C5), 9427–9434. https://doi.org/10.1029/2000JC900155

DiGiacomo, P. M., & Holt, B. (2001). Satellite observations of small coastal ocean eddies in the Southern California Bight. *Journal of Geophysical Research*, *106*(C10), 22521–22543. https://doi.org/10.1029/2000jc000728

Durski, S. M., & Allen, J. S. (2005). Finite-amplitude evolution of instabilities associated with the coastal upwelling front. *Journal of Physical Oceanography*, *35*(9), 1606–1628. https://doi.org/10.1175/JPO2762.1

Edson, J., Crawford, T., Crescenti, J., Farrar, T., Frew, N., Gerbi, G., et al. (2007). The coupled boundary layers and air—Sea transfer experiment in low winds. *Bulletin of the American Meteorological Society*, *88*(3), 341–356. https://doi.org/10.1175/BAMS-88-3-341

Ferrari, R., & Nikurashin, M. (2010). Suppression of eddy diffusivity across jets in the southern ocean. *Journal of Physical Oceanography*, *40*(7), 1501–1519. https://doi.org/10.1175/2010JPO4278.1

Fewings, M., & Lentz, S. J. (2011). Summertime cooling of the shallow continental shelf. *Journal of Geophysical Research*, *116*. C07015. https://doi.org/10.1029/2010JC006

Flament, P., & Armi, L. (2000). The shear, convergence, and thermohaline structure of a front. *Journal of Physical Oceanography*, *30*(1), 51–66. https://doi.org/10.1175/1520-0485(2000)030<0051:tscats>2.0.co;2

Fratantoni, P. S., & Pickart, R. S. (2003). Variability of the shelf break jet in the Middle Atlantic Bight: Internally or externally forced? *Journal of Geophysical Research*, *108*(C5), 3166. https://doi.org/10.1029/2002JC001326

Ganju, N. K., Lentz, S. J., Kirincich, A. R., & Farrar, J. T. (2011). Complex mean circulation over the inner-shelf south of Martha's Vineyard revealed by observations and a high-resolution model. *Journal of Geophysical Research*, *116*(C10), C10036. https://doi.org/10.1029/2011JC007,035

He, R., & Wilkin, J. L. (2006). Barotropic tides on the southeast New England shelf: A view from a hybrid data assimilative modeling approach. *Journal of Geophysical Research*, *111*(C8). C08002. https://doi.org/10.1029/2005JC003

Hoskins, B. J., & Bretherton, F. P. (1972). Atmospheric frontogenesis models: Mathematical formulation and solution. *Journal of the Atmospheric Sciences*, *29*(1), 11–37. https://doi.org/10.1175/1520-0469(1972)029<0011:afmmfa>2.0.co;2

Hoskins, B. J., & West, N. V. (1979). Baroclinic waves and frontogenesis. Part II: Uniform potential vorticity jet flows-cold and warm fronts. *Journal of the Atmospheric Sciences*, *36*, 1663–1680. https://doi.org/10.1175/1520-0469(1979)036<1663:bwafpi>2.0.co;2

Kim, S. Y. (2010). Observations of submesoscale eddies using high-frequency radar-derived kinematic and dynamic quantities. *Continental Shelf Research*, *30*(15), 1639–1655. https://doi.org/10.1016/j.csr.2010.06.011

Kim, S. Y., Terrill, E., & Cornuelle, B. (2007). Objectively mapping {HF} radar-derived surface current data using measured and idealized data covariance matrices. *Journal of Geophysical Research*, *112*(C6), C06021. https://doi.org/10.1029/2006JC003756

Kim, S. Y., Terrill, E. J., Cornuelle, B. D., Jones, B., Washburn, L., Moline, M. A., et al. (2011). Mapping the U.S. West coast surface circulation: A multiyear analysis of high-frequency radar observations. *Journal of Geophysical Research*, *116*(C3), C03011. https://doi.org/10.1029/2010JC006669

Kirincich, A. R. (2016b). The occurrence, drivers, and implications of submesoscale eddies on the martha's vineyard inner shelf. *Journal of Physical Oceanography*, *46*(9), 2645–2662. https://doi.org/10.1175/JPO-D-15-0191.1

Kirincich, A. R. (2016a). Remote sensing of the surface wind field over the coastal ocean via direct calibration of HF radar backscatter power. *Journal of Atmospheric and Oceanic Technology*, *33*(7), 1377–1392. https://doi.org/10.1175/JTECH-D-15-0242.1

Kirincich, A. R., Emery, B., Washburn, L., & Flament, P. (2019). Improving surface current resolution using direction finding algorithms for multiantenna high-frequency radars. *Journal of Atmospheric and Oceanic Technology*, *36*(10), 1997–2014. https://doi.org/10.1175/JTECH-D-19-0029.1

Kirincich, A. R., & Lentz, S. J. (2017). The importance of lateral variability on exchange across the inner shelf south of Martha's Vineyard, MA. *Journal of Geophysical Research: Oceans*, *122*(3), 2360–2381. https://doi.org/10.1002/2016JC012491

Kirincich, A. R., Lentz, S. J., Farrar, J. T., & Ganju, N. K. (2013). The spatial structure of tidal and mean circulation over the inner shelf south of Martha's Vineyard, Massachusetts. *Journal of Physical Oceanography*, *43*(9), 1940–1958. https://doi.org/10.1175/JPO-D-13-020.1

Klymak, J. M., Crawford, W., Alford, M. H., MacKinnon, J. A., & Pinkel, R. (2015). Along-isopycnal variability of spice in the North Pacific. *Journal of Geophysical Research: Oceans*, *120*(3), 2287–2307. https://doi.org/10.1002/2013JC009421

Kunze, E., Klymak, J. M., Lien, R.-C., Ferrari, R., Lee, C. M., Sundermeyer, M. A., & Goodman, L. (2015). Submesoscale water-mass spectra in the sargasso sea. *Journal of Physical Oceanography*, *45*(5), 1325–1338. https://doi.org/10.1175/JPO-D-14-0108.1

LaCasce, J. H. (2008). Statistics from Lagrangian observations. *Progress in Oceanography*, *77*(1), 1–29. https://doi.org/10.1016/j.pocean.2008.02.002

Lapeyre, G., & Klein, P. (2006). Dynamics of the upper oceanic layers in terms of surface quasigeostrophy theory. *Journal of Physical Oceanography*, *36*(2), 165–176. https://doi.org/10.1175/JPO2840.1

Lentz, S. J. (2010). The mean along-isobath heat and salt balances over the middle atlantic Bight continental shelf. *Journal of Physical Oceanography*, *40*(1976), 934–948. https://doi.org/10.1175/2009JPO4214.1

Lentz, S. J. (2017). Journal of geophysical research : Oceans seasonal warming of the middle atlantic Bight cold pool. *Journal of Geophysical Research: Oceans*, *122*(2), 941–954. https://doi.org/10.1002/2016JC012201.Received

Lentz, S. J., Fewings, M., Howd, P., Fredericks, J., & Hathaway, K. (2008). Observations and a model of undertow over the inner continental shelf. *Journal of Physical Oceanography*, *38*(11), 2341–2357. https://doi.org/10.1175/2008JPO3986.1

Lentz, S. J., & Fewings, M. R. (2012). The wind- and wave-driven inner-shelf circulation. *Annual Review of Marine Science*, *4*(1), 317–343. https://doi.org/10.1146/annurev-marine-120709-142745

Limeburner, R., & Beardsley, R. (1982). The seasonal hydrography and circulation over Nantucket shoals. *Journal of Marine Research*, *40*, 371–406.

Mahadevan, A., D'Asaro, E., Lee, C., & Perry, M. J. (2012). Eddy-driven stratification initiates north atlantic spring phytoplankton blooms. *Science*, *337*(6090), 54–58. https://doi.org/10.1126/science.1218740

Mahadevan, A., & Tandon, A. (2006). An analysis of mechanisms for submesoscale vertical motion at ocean fronts. *Ocean Modelling*, *14*(3–4), 241–256. https://doi.org/10.1016/j.ocemod.2006.05.006

Mahadevan, A., Thomas, L. N., & Tandon, A. (2008). Comment on "Eddy/wind interactions stimulate extraordinary mid-ocean plankton blooms". *Science (New York, N.Y.)*, *320*(5875), 448. author reply 448. https://doi.org/10.1126/science.1152111

McCabe, R. M., MacCready, P., & Pawlak, G. (2006). Form drag due to flow separation at a headland. *Journal of Physical Oceanography*, *36*(11), 2136–2152. https://doi.org/10.1175/JPO2966.1

Mcwilliams, J. C. (1985). Submesoscale, coherent vorticities in the ocean. *Reviews of Geophysics*, *23*(2), 165–182. https://doi.org/10.1029/rg023i002p00165

McWilliams, J. C. (2009). Targeted coastal circulation phenomena in diagnostic analyses and forecasts. *Dynamics of Atmospheres and Oceans*, *48*(1–3), 3–15. https://doi.org/10.1016/j.dynatmoce.2008.12.004

McWilliams, J. C. (2016). Submesoscale currents in the ocean. *Proceedings of Royal Society A*, *472*(2189), 20160117. https://doi.org/10.1098/rspa.2016.0117

Molemaker, M. J., McWilliams, J. C., & Yavneh, I. (2005). Baroclinic instability and loss of balance. *Journal of Physical Oceanography*, *35*(9), 1505–1517. https://doi.org/10.1175/JPO2770.1

Nencioli, F., Dong, C., Dickey, T., Washburn, L., & Mcwilliams, J. C. (2010). A vector geometry-based eddy detection algorithm and its application to a high-resolution numerical model product and high-frequency radar surface velocities in the Southern California Bight. *Journal of Atmospheric and Oceanic Technology*, *27*(3), 564–579. https://doi.org/10.1175/2009JTECHO725.1

Ohlmann, C., White, P., Washburn, L., Terrill, E., Emery, B., & Otero, M. (2007). Interpretation of coastal HF radar–derived surface currents with high-resolution drifter data. *Journal of Atmospheric and Oceanic Technology*, *24*(4), 667–680. https://doi.org/10.1175/jtech1998.1

Okubo, A. (1971). Oceanic diffusion diagram. *Deep Sea Research II*, *18*(8), 789–802. https://doi.org/10.1016/0011-7471(71)90046-5

Paduan, J. D., & Niiler, P. P. (1990). A Lagrangian description of motion in northern California coastal transition filaments. *Journal of Geophysical Research*, *95*(C10), 18095–18109. https://doi.org/10.1029/jc095ic10p18095

Pawlowicz, R., Beardsley, B., & Lentz, S. (2002). Classical tidal harmonic analysis including error estimates in MATLAB using T_TIDE. *Computers & Geosciences*, *28*(8), 929–937. https://doi.org/10.1016/s0098-3004(02)00013-4

Priestley, M. (1981). *Spectral analysis and time series* (p. 890). Academic Press.

Rocha, C., Chereskin, T. K., Gille, S., & Menemenlis, D. (2016). Mesoscale to submesoscale wavenumber spectra in drake passage. *Journal of Physical Oceanography*, *46*(2), 601–620. https://doi.org/10.1175/JPO-D-15-0087.1

Romero, L., Uchiyama, Y., Ohlmann, J. C., McWilliams, J. C., & Siegel, D. a. (2013). Simulations of nearshore particle-pair dispersion in southern California. *Journal of Physical Oceanography*, *43*(9), 1862–1879. https://doi.org/10.1175/JPO-D-13-011.1

Rudnick, D. L., & Cole, S. T. (2011). On sampling the ocean using underwater gliders. *Journal of Geophysical Research*, *116*(C8), C08010. https://doi.org/10.1029/2010JC006849

Rypina, I., Kirincich, A. R., Lentz, S., & Sundermeyer, M. (2016). Investigating the eddy diffusivity concept in the coastal ocean. *Journal of Physical Oceanography*, *46*(7), 2201–2218. https://doi.org/10.1175/jpo-d-16-0020.1

Rypina, I. I., Kirincich, A. R., Limeburner, R., & Udovydchenkov, I. A. (2014). Eulerian and Lagrangian correspondence of high-frequency radar and surface drifter data: Effects of radar resolution and flow components. *Journal of Atmospheric and Oceanic Technology*, *31*(4), 945–966. https://doi.org/10.1175/JTECH-D-13-00146.1

Scott, R. B., & Wang, F. (2005). Direct evidence of an oceanic inverse kinetic energy cascade from satellite altimetry. *Journal of Physical Oceanography*, *35*(9), 1650–1666. https://doi.org/10.1175/JPO2771.1

Serra, M., Sathe, P., Rypina, I., Kirincich, A. R., Ross, S. D., Lermusiaux, P., et al. (2020). Search and rescue at sea aided by hidden flow structures. *Nature Communications*, *11*(1), 2525. https://doi.org/10.1038/s41467-020-16281-x

Signell, R. P., & Geyer, W. R. (1991). Transient eddy formation around headlands. *Journal of Geophysical Research*, *96*(C2), 2561–2575. https://doi.org/10.1029/90jc02029

Sinnett, G., & Feddersen, F. (2014). The surf zone heat budget: The effect of wave heating. *Geophysical Research Letters*, *41*(20), 7217–7226. https://doi.org/10.1002/2014GL061398

Soh, H. S., & Kim, S. Y. (2018). Diagnostic characteristics of submesoscale coastal surface currents. *Journal of Geophysical Research: Oceans*, *123*(3), 1838–1859. https://doi.org/10.1002/2017JC013428

Spiro Jaeger, G., Mackinnon, J. A., Lucas, A. J., Shroyer, E., Nash, J., Tandon, A., et al. (2020). How spice is stirred in the Bay of Bengal. *Journal of Physical Oceanography*, *50*(9), 2669–2688. https://doi.org/10.1175/JPO-D-19-0077.1

Spydell, M., Feddersen, F., Guza, R. T., & Schmidt, W. E. (2007). Observing surf-zone dispersion with drifters. *Journal of Physical Oceanography*, *37*(12), 2920–2939. https://doi.org/10.1175/2007JPO3580.1

Sundermeyer, M., & Ledwell, J. (2001). Lateral dispersion over the continental shelf: Analysis of dye release experiments. *Journal of Geophysical Research*, *106*(C5), 9603–9621. https://doi.org/10.1029/2000jc900138

Thomas, L., & Lee, C. (2005). Intensification of ocean fronts by down-front winds. *Journal of Physical Oceanography*, *35*(6), 1086–1102. https://doi.org/10.1175/jpo2737.1

Thomas, L. N., Tandon, A., & Mahadevan, A. (2008). Submesoscale processes and dynamics. In M. W. Hecht, & H. Hasumi (Eds.), *Ocean modeling in an eddying regime*, *17–38* (pp. 17–38). American Geophysical Union. https://doi.org/10.1029/177GM04

Thompson, A. F., Lazar, A., Buckingham, C., Naveira Garabato, A. C., Damerell, G. M., & Heywood, K. J. (2016). open-ocean submesoscale motions: A full seasonal cycle of mixed layer instabilities from gliders. *Journal of Physical Oceanography*, *46*(4), 1285–1307. https://doi.org/10.1175/jpo-d-15-0170.1

Ullman, D. S., & Cornillon, P. C. (2001). Continental shelf surface thermal fronts in winter off the northeast US coast. *Continental Shelf Research*, *21*(11–12), 1139–1156. https://doi.org/10.1016/S0278-4343(00)00107-2

Wilkin, J. (2006). The summertime heat budget and circulation of southeast New England shelf waters. *Journal of Physical Oceanography*, *36*(11), 1997–2011. https://doi.org/10.1175/jpo2968.1

Yoo, J. G., Kim, S. Y., & Kim, H. S. (2018). Spectral descriptions of submesoscale surface circulation in a coastal region journal of geophysical research : Oceans. *Journal of Geophysical Research: Oceans*, *123*(6), 4224–4249. https://doi.org/10.1029/2016JC012517